Association of rocks with different P-T paths within the Barchi-Kol UHP terrain (Kokchetav Complex): Implications for subduction and exhumation of continental crust

Revision 1

Aleksandr S. Stepanov[1,2]

Daniela Rubatto[1,3]

Joerg Hermann[1,3]

Andrey V. Korsakov[4]

1: Research School of Earth Sciences, The Australian National University, Canberra, 2601 ACT, Australia

2: CODES, University of Tasmania, Private Bag 79, Hobart, Tasmania 7001, Australia.

3: now at Institute of Geological Sciences, University of Bern, 3012 Bern, Switzerland

4: V.S. Sobolev Institute of Geology and Mineralogy of Siberian Branch of Russian Academy of Sciences, Koptyug Pr. 3, Novosibirsk 630090, Russia

Corresponding author: Aleksandr S. Stepanov.

The Barchi-Kol terrain is a classic locality of ultrahigh pressure (UHP) metamorphism within the Kokchetav metamorphic belt. We provide a detailed and systematic characterization of four metasedimentary samples using main mineral assemblages, mineral inclusions in zircon and monazite, garnet major and trace element zoning as well as Zr-in-rutile and Ti-in-zircon

temperatures. A typical diamond-bearing gneiss records peak conditions of 49±4 kbar and 950–1000°C. Near isothermal decompression of this rock resulted in the breakdown of phengite associated with a nearly pervasive recrystallization of the rock. The same terrain also contains micaschists that experienced peak conditions close to those of the diamond bearing rocks, but they were exhumed along a cooler path where phengite remained stable. In these rocks, major and trace element zoning in garnet has been completely equilibrated. A layered gneiss was metamorphosed at UHP conditions in the coesite field, but did not reach diamond-facies conditions (peak conditions: 30 kbar and 800–900°C). In this sample, garnet records retrograde zonation in major elements but also retains prograde zoning in trace elements. A garnet-kyanite-micaschist that equilibrated at significantly lower pressures (24±2 kbar, 710±20°C) contains garnet with major and trace element zoning. The diverse garnet zoning in samples that experienced different metamorphic conditions allows to establish that diffusional equilibration of rare earth element in garnet likely occurs at ~900–950°C. Different metamorphic conditions in the four investigated samples are also documented in zircon trace element zonation and mineral inclusions in zircon and monazite.

U-Pb geochronology of metamorphic zircon and monazite domains demonstrates that prograde (528–521 Ma), peak (528–522 Ma) and peak to retrograde metamorphism (503–532 Ma) occurred over a relatively short time interval that is indistinguishable from metamorphism of other UHP rocks within the Kokchetav metamorphic belt. Therefore, the assembly of rocks with contrasting P-T trajectories must have occurred in a single subduction-exhumation cycle, providing a snapshot of the thermal structure of a subducted continental margin prior to collision. The rocks were initially buried along a low geothermal gradient. At 20–25 kbar they underwent near isobaric heating of 200°C, which was followed by continued burial along a low geothermal gradient. Such a stepped geotherm is in good agreement with predictions from subduction zone thermal models.

Key words: UHP, accessory minerals, REE, metamorphic path, subduction, exhumation

Introduction

Ultra-high pressure (UHP) metamorphic terrains document processes during subduction and exhumation of oceanic and continental crust to extreme conditions, and are crucial for the investigation of release of fluids and melts that transport elements from the subducted crust to the mantle beneath island arcs (Plank and Langmuir 1998; Bebout et al. 1999; Hermann and Rubatto 2012; Stepanov et al. 2014). In order to harvest the wealth of information stored in UHP rocks it is essential to distinguish between mineral assemblages formed during different stages of subduction and exhumation of these rocks (Peterman et al. 2009). Additionally, UHP terrains are found in complex accretionary and collisional belts that may also include lower pressure rocks and thus it is essential to discriminate between UHP rocks and rocks formed at crustal pressure (Dobretsov et al. 1995; Kaneko et al. 2000; Forster et al. 2004; Peterman et al. 2009). Not surprisingly, the pressure-temperature-time (P-T-t) histories of UHP and surrounding rocks are difficult to reconstruct due to intensive retrogression during exhumation and homogenization of mineral compositions by diffusion or recrystallization, processes that erase information on prograde to peak metamorphic conditions (Hermann and Rubatto 2014). Rocks with UHP mineral assemblages might appear as small blocks surrounded by country rocks that have non-UHP mineral associations (Liu et al. 2007; Peterman et al. 2009). The most common explanations of these phenomena are pervasive retrograde alteration (Sobolev et al. 1991) or preservation of metastable assemblages during UHP metamorphism (Peterman et al. 2009). Alternatively, the surrounding country rocks might not have experienced the same metamorphic history as the nearby UHP units. The most complete record of UHP metamorphism is often contained in inclusions in robust minerals such as garnet and zircon (Sobolev et al. 1991; Hermann et al. 2001; Liu et al. 2002), but it is difficult to reconstruct metamorphic paths from inclusion assemblages alone. Thus, there is a need to develop additional tools to characterize the P-T evolution of UHP rocks. Particularly interesting are systems that are characterized by slow diffusion such as Ti-in-zircon and Zr-in-rutile thermometry and garnet, zircon and monazite REE patterns as they have a better chance of surviving extreme metamorphic temperatures.

The Kokchetav metamorphic belt in northern Kazakhstan is known for its UHP metamorphic rocks, which host abundant metamorphic microdiamonds and other indicators of extremely high pressures. Numerous studies have shown that the Kokchetav rocks were subducted to a depth of more than 120 km and then exhumed to the surface (Dobretsov et al. 1995; Kaneko et al. 2000; Schertl and Sobolev 2013). The peak conditions are estimated to reach 45–70 kbar and 950–1000°C (Sobolev and Shatsky 1990; Ogasawara et al. 2002; Chopin 2003) at 530–520 Ma (Claoue-Long et al. 1991; Hermann et al. 2001; Ragozin et al. 2009). Beside the famous UHP units of Kumdi-Kol, Barchi-Kol and Kulet, the Kokchetav complex, also contains units that record more moderate conditions to low pressure metamorphism in the Daulet suite (Dobretsov et al. 2006; Buslov et al. 2010; Zhimulev et al. 2010). Previous tectonic models of the Kokchetav region considered the UHP terrains as coherent units with consistent peak metamorphic conditions and the same exhumation path (Kaneko et al. 2000). In such reconstructions the UHP rocks have tectonic contacts with lower pressure rocks (Dobretsov et al. 1995; Kaneko et al. 2000). Alternatively the

UHP rocks have also been described as part of a "mega-melange" (Dobrzhinetskaya et al. 1994; Dobretsov et al. 1995).

In this contribution we investigate in detail four metapelite samples from the Barchi-Kol UHP unit using major and trace element compositions of major and accessory phases. We compare this information with P-T conditions extracted from mineral inclusions in zircon and monazite and then evaluate to what extent major and trace element signatures are retained in UHP minerals. This petrologic investigation is complemented by a comprehensive geochronological study to demonstrate that all investigated rocks formed during the same subduction cycle. Based on these data we demonstrate that the Barchi-Kol UHP unit contains rocks with different metamorphic paths and peak conditions and discuss the implications of this finding for the thermal structure of subducted continental margins.

Geologic setting

Kokchetav complex

The Kokchetav metamorphic belt (KMB, also known as Kokchetav complex or massif) is located in northern Kazakhstan (Fig. 1a). The KMB is a part of the Central Asia fold belt, which covers thousands of kilometers between the East European, Siberian, North China and Tarim cratons (Zonenshain et al. 1990; Wang et al. 2011). The Central Asia fold belt is comprised of Paleozoic continental crust, which is itself composed of oceanic arcs, sedimentary complexes and blocks of Precambrian continental crust separated by ophiolites, sometimes with high pressure rocks (Dobretsov and Buslov 2007; Zhimulev et al. 2010, 2011; Glorie et al. 2015) and intruded by abundant granitic intrusions. The KBM represents one of these ancient blocks. Arcs formed during the early Paleozoic (Caledonian orogeny, 490–390 Ma), were assembled by collisional events during the Hercynian–Variscan orogeny (380–280 Ma) and the belt was completed in the Permian (Zonenshain et al. 1990). The Kokchetav complex has an Early–Mid Cambrian age (Claoue-Long et al. 1991; Hermann et al. 2001) and it is surrounded by younger Paleozoic structures (Dobretsov and Buslov 2007; Buslov et al. 2009; Zhimulev et al. 2011).

The Kokchetav metamorphic belt extends from E-NE to W-SW over 150 km, with boundaries defined by younger terrains. The southern boundary of the Kokchetav complex is defined by the Zerenda granite batholith. North of the Kokchetav complex is the North Kokchetav tectonic zone, while further North, the Stepnyak paleo-island arc crops out. The North Kokchetav tectonic zone is composed of thrust sheets of low grade rocks, lenses of HP rocks, and contains olistostrome formations, which demonstrate sedimentation during orogenesis (Zhimulev et al. 2010, 2011). The North Kokchetav tectonic zone formed due to collision of the Kokchetav microcontinent and the Stepnyak paleo-island arc in Early to Middle Ordovician, substantially later than the Early–Middle Cambrian age of the Kokchetav metamorphic complex. The Stepnyak paleo-island arc is composed of low grade sediments and volcanic formations (Zhimulev et al. 2010, 2011).

The Kokchetav complex is composed of units with different metamorphic conditions, which researchers have named suites, domains and/or terrains (Rozen 1971). The dominant lithologies are low grade Precambrian sedimentary rocks, which are interpreted as sedimentary cover of the Kokchetav microcontinent, and felsic gneisses exposed in several localities as its basement (Dobrzhinetskaya et al. 1994; Dobretsov et al. 1995; Turkina et al. 2011). Within these Precambrian suits are tectonically juxtaposed HP and UHP terrains (from west to east): Barchi-Kol, Kumdy-Kol, Sulu Tjube, Enbek Berlyk, and Kulet. UHP rocks are exposed in Kulet, Kumdy-Kol, Barchi-Kol and there have been reports of findings of diamond-bearing rocks further South-West of the Barchi-Kol area (Shatsky et al. 2005). Kumdy-Kol and Bachi-Kol reached sufficiently high pressures to stabilize diamond and peak temperatures are estimated at 950–1000°C, whereas in the Kulet area, metamorphism occurred in the stability field of coesite at lower temperatures of 720–760°C (Parkinson 2000).

There are two general interpretations of the regional structure of the Kokchetav metamorphic belt. One is the "transpressional" or "mega-melange" model proposed by Russian geologists (Dobrzhinetskaya et al. 1994; Dobretsov et al. 1995). Another interpretation is the extrusion wedge "subhorizontal model" (Kaneko et al. 2000), in which the primary structure of the Kokchetav complex is sub-horizontal and layered and the UHP rocks are “telescoped” into envelops of units with progressively lower peak metamorphic conditions during exhumation along a subduction channel.

Barchi-Kol unit

The most renowned UHP locality in the Kokchetav complex is Kumdy-Kol, where an exploration audit has excavated abundant UHP rocks. The Barchi-Kol UHP unit is located 17 km west of the Kumdy-Kol UHP unit near Barchi-Kol Lake. It is elongated from southwest to northeast and has a size of approximately 2.5×5 km (Fig. 1b). The Barchi-Kol UHP metamorphic unit is bound in the northwest and north by faults separating the UHP rocks from the weakly metamorphosed Precambrian sediments of the Kokchetav and Sharyk suites. To the South of this UHP unit occurs the Krasnomai alkali-utrabasic complex, composed of pyroxenites, micaceous pyroxenites and carbonatites that intruded at 464±30 Ma according to Rb-Sr dating (Letnikov et al. 2004).

The internal structure of the Barchi-Kol unit is known from the mapping and drilling carried out by the Kokchetav Prospecting Expedition (Fig. 1b), the Kokchetav geological survey and surface mapping by Masago (2000). In the Barchi-Kol unit, rocks dip steeply to the South-East at 70°. The following rock types are described in the Barchi-Kol area: eclogites, garnet-pyroxenites, amphibolites, calc-silicates, migmatites, schists and a variety of gneisses. The most abundant rock type is a gneiss composed of feldspars, quartz and garnet. Based on their subordinate mineral phases, gneisses can be subdivided into kyanite, clinopyroxene, clinozoisite, biotite, and two-mica bearing varieties (Lavrova et al. 1996; Korsakov et al. 2002). The calcsilicate rocks are interlayered with garnet-biotite gneisses. Eclogites and amphibolites occur as boudins in a matrix of gneisses and schists. A peculiar rock type of the Barchi-Kol unit is clinozoisite gneiss, which is often diamondiferous (Korsakov et al. 2002, 2006). The lithologies are variable and it is hard to trace any particular layer from one drill core to another (Korsakov et al. 2002).

Metabasites outcropping in the Barchi-Kol area have been mapped in three zones with different metamorphic conditions (Masago 2000): in zone D rocks achieved UHP conditions estimated at 27–40 kbar, 700–825°C; and in zones B and C peak metamorphic conditions were much lower at 11.7± 0.5 kbar, 700± 30°C and 12–14 kbar, 700–815°C, respectively (Fig. 1b). Zone D of Masago (2000) broadly coincides with the UHP terrain constrained by the Kokchetav Prospecting Expedition. Samples for this study were collected in the northern part of the UHP terrain, which contains a high proportion of eclogites, the central section, which has abundant gneisses, and the southern section dominated by granites and orthogneisses (Fig. 1b).

8

Analytical methods

Phase relations were analyzed in polished thin sections using an optical microscope and back-scattered electron (BSE) images on a JEOL 6400 scanning electron microscope (SEM) (Electron Microscopy Unit, ANU). The phase compositions were determined by EDS SEM, using an acceleration voltage of 15 kV, a beam current of 1 nA and an acquisition time of 120 s. Distribution of major and trace elements in thin sections was mapped with a Cameca SX100 microprobe. Fe, Mg, Mn, Y and P in garnet were measured using WDS spectrometers, with Ca simultaneously analyzed by EDS. The probe current and accelerating voltage were 100 nA and 15 kV, respectively. The acquisition time for garnet maps was from 2 to 12 hours allowing detection of P and Y zoning at the 1000 ppm level. Mineral inclusions in zircon and monazite were analyzed by SEM-EDS analyses that were carefully checked for contributions from the host mineral. Zoning of monazite was identified by high-contrast backscatter electron (BSE) imaging using a Cambridge S360 scanning electron microscope (SEM) at the ANU Electron Microscopy Unit (2 nA, 15 kV and 15 mm working distance). Cathodoluminescence (CL) imaging of zircon was carried out on a Hitachi S2250N SEM fitted with an ellipsoidal mirror for CL at the ANU Electron Microscopy Unit.

Trace elements in minerals were analyzed by LA-ICP-MS at the Research School of Earth Sciences, ANU, using a pulsed 193 nm Ar-F Excimer laser with 100 mJ source energy at a repetition rate of 5 Hz (Eggins et al. 1998) coupled to an Agilent 7500 quadrupole ICP-MS. Laser sampling was performed in a He–Ar–H_2 atmosphere using a spot diameter of 25–37 μm. Data acquisition was performed by peak hopping in pulse counting mode, acquiring individual intensity data for each element during each mass spectrometer sweep. A total of 60 s, comprising a gas background of 20–25 s and 30–35 s signal, were acquired for each analysis. Laser data were processed with an Excel spreadsheet created by Charlotte Allen. Trace element data in garnet was calculated with NIST 612 (Pearce et al. 1997) as the external standard and SiO_2 as the internal standard. Monazite, rutile and zircon were calculated with NIST 610 (Pearce et al. 1997) as the external standard and Ce, Ti and SiO_2 as the internal standards, respectively. LA-ICP-MS of monazite with very low HREE content demonstrated apparent positive anomalies of Er^{166} and Yb^{172} on chondrite normalized patters. They were interpreted as interferences with oxides of Nd^{150} and Gd^{156} or Ce^{140} dioxide, which are abundant in LREE-rich monazite. Therefore Er and Yb were calculated from geometric averages of the adjacent rare earths. BCR-2 glass was employed as secondary standard and its composition was reproduced within 5 % (Norman et al. 1998).

Raman spectra were obtained at Geoscience Australia, Canberra under the supervision of Terry Mernagh. The Raman equipment comprises a Dilor SuperLabram spectrometer, with a holographic notch filter (600 and 1800 g/mm gratings), liquid nitrogen-cooled 2000 pixel CCD detector, and a 514.5 nm Melles Griot 543 argon ion laser (5 mW at the sample). The spectral resolution was set at 2 cm^{-1} (slit width of 100 μm). The microscope uses a 50X ULWD Olympus microscope objective, focusing the laser spot to 2 μm in diameter and 5 μm deep.

U, Th–Pb isotope analyses of zircon and monazite were performed using the sensitive, high-resolution ion microprobes at the RSES (SHRIMP II and RG) using a 3.5–4.0 nA, 10 kV primary O^{-2} beam focused through a 120 μm aperture to form a 25 *μm* diameter spot. Data acquisition followed Williams (1998) and data were collected as sets of six scans throughout the mass range. For monazite, energy filtering was used to eliminate interferences on ^{204}Pb, as described by Rubatto et al. (2001). The common Pb correction was based on the measured ^{204}Pb for monazite assuming the Broken Hill common Pb composition (Williams 1998). The ^{208}Pb common lead correction was applied for zircon because it contained much lower Th content than in monazite resulting in a low content of radiogenic ^{208}Pb. The measured $^{206}Pb/^{238}U$ ratios were corrected using reference monazite 44069 (425 Ma) and TEMORA zircon (417 Ma). Ages were calculated using Isoplot and SQUID software (Ludwig 2003). Calibration error for each session was between 1 and 2.4 % and was propagated to individual analyses. Individual measurements are given with 1σ error and averages are reported at 95% confidence level. In order to account for external errors, any uncertainty on average ages that was below 1% was increased to 1%.

Sample description

We investigated a typical UHP garnet-biotite gneiss (B118A50) containing diamonds, as well as less common metasedimentary samples (B94-333, B94-256 and B01-3). The metasediments show some peculiar features, such as large garnet porphyroblasts (B94-333) and high abundance of white mica (B94-256, B01-3). Three samples (B94-333, B94-256 and B118A50) are from drill cores and one sample (B01-3) was collected from the surface in the western part of the Barchi-Kol lake area (Fig. 1b).

In order to constrain their metamorphic evolution the samples were systematically investigated for major element composition of white mica and major and trace element zoning in garnet, zircon and monazite and mineral inclusions in these phases. U-Pb ages of monazite and zircon were determined by SHRIMP analysis. The information obtained by these methods, including the full assemblages, is summarized in Table 1 and the relative crystallization sequence for each sample is shown in Supplementary Figure 1.

11

B01-3 is a weakly foliated micaschist of metapelitic composition composed of garnet, phengite, quartz and kyanite (Fig. 2a). Phengite occurs as large flakes forming the foliation of the rock. Biotite is a minor constituent and it is associated with garnet and phengite rims. Grains of kyanite are small and often have irregular, resorbed shapes and are enclosed in phengite. Garnet crystals are euhedral and have a bimodal distribution in size: either >3 mm or <0.5 mm (Fig. 2a). Large garnet crystals have cores crowded with small monocrystalline inclusions of quartz and occasionally xenotime (Fig. 2b). There are small inclusions of zircon, apatite rutile and phengite in garnet mantles, as well as polyphase inclusions with the associations of quartz, chlorite, K-feldspar, phengite, rutile, ilmenite and xenotime. Garnet rims have no inclusions. Inclusions in monazite mostly occur at the boundary between core and rims domains and represent the same association as the matrix of the sample (kyanite, garnet, phengite, zircon and rutile). Zircons from sample B01-3 contain inclusions of quartz, garnet and phengite, which unfortunately were too small for analysis.

B94-333 is a garnet-biotite gneiss with thin layers (2-4 mm) composed of quartz-feldspars and darker layers enriched in biotite (Fig. 2c–d). One such layer contains abundant grains of rounded kyanite, whereas, in other parts of the sample kyanite is absent. Another layer contains several large, elongated grains of pink garnet (up to 9×5 mm), which are associated with pressure shadows filled with quartz and feldspars. Another layer is composed of orange garnet, biotite, quartz and contains allanite. Grains of pink garnet contain inclusions of rutile in the mantle and monazite inclusions close to the rim (Fig. 2e). Zircons contain inclusions of garnet, clinopyroxene, phengite and coesite was identified with Raman spectroscopy. Monazites contain inclusions of phengite and garnet.

12

B94-256 is a foliated micaschist of metasedimentary composition composed of garnet, quartz, phengite, biotite and K-feldspar (Fig. 2f-g). Garnet grains are approximately 2 mm in size and phengite crystals are 0.5–1 mm across and elongated along the foliation. Biotite occurs as small randomly oriented grains along the edges of phengite and garnet. Zircon and monazite form large grains (often >200 μm) dispersed in the matrix and monazite occasionally has a corona of apatite. Rutile is present only as inclusions in garnet and is absent in the matrix (Fig. 2h). Garnet contains inclusions of rutile, phengite and biotite. Biotite replaces garnet rims and phengite grains and inclusions of phengite (Fig. 2h), and thus biotite is interpreted as a retrograde mineral. Monazite contains inclusions of K-feldspar, biotite, and phengite. Zircons contain inclusions of phengite, garnet, rutile and coesite.

The diamondiferous B118A50 gneiss has thin (2-3 mm) quartz-feldspatic layers and layers enriched in garnet and biotite (Fig. 2i). Garnet grains (≈2 mm) are often fractured and surrounded by biotite and chlorite. Both biotite and phengite are oriented along foliation and significantly altered: biotite contains needles of rutile and is partially replaced by chlorite; phengite is surrounded by chlorite rims. K-Feldspars grains are small (50-100μm), have an irregular shape and significantly altered. Plagioclase is more abundant than K-feldspar and is altered to fine grained mica. Quartz grains have irregular shape and undulose extinction. The rock contains large grains of rutile aligned with the foliation, which are partly altered (Fig. 2j–k). Also aligned with the foliation are aggregates of phengite and Th-REE minerals, which are pseudomorphs after allanite (Stepanov et al. 2014). Zircon contains inclusions of diamond, garnet, clinopyroxene, phengite and biotite. Inclusions of metamorphic diamonds are present in CL-bright mantle zones (which also have the highest Ti-in-zircon temperatures, see below) of the zircon and at the boundaries between these zones and CL-dark cores (Fig. 2k).

Mineral compositions

Minerals were analyzed in thin sections and mineral inclusions were investigated in garnet (in thin sections) and in monazite and zircon (in mounted mineral separates), which are known as robust containers for inclusions that document the HP history.

In Ky-bearing micaschist B01−3, garnet grains have extensive growth zoning in major and trace elements (Fig. 3, 4, 5, 6, 7): large grains have cores with elevated Mn ($Alm_{83.5–86}$, $Py_{6.5–8}$, $Grs_{5–5.5}$, $Sps_{2.5–3.1}$), surrounded by mantles with lower Mn content ($Alm_{81–86}$, $Py_{8–13}$, $Grs_{4.6–5}$, $Sps_{1.2}$) and the rims with Mn and Fe decrease accompanied by Ca and Mg increase ($Alm_{74–78}$, $Py_{13–17}$, $Grs_{7–8}$, $Sps_{0.2–0.9}$). The rim composition is identical to the composition of small garnet grains (Fig. 5 and Table S1). HREE and Y concentrations decrease by a factor of 80 from garnet core to rim (Fig. 4). Garnet core and mantle REE patterns have a negative Eu anomaly (Eu/Eu^*=0.1), which is reduced in the rims (Eu/Eu^*=0.5−0.6). Garnet inclusions in monazite have a composition similar to that of the rims of large garnets (low Mn, high Mg and Ca, Fig. 5). Large phengite grains display a decrease of Si and Mg content and an increase of Ti from core to rim (Fig. 3). The TiO_2 content is below 1 wt%. Phengite inclusions in garnet mantles have compositions similar to phengite cores. One monazite core includes phengite grains with 3.08–3.11 Si pfu, which are lower in Si than most of the white mica in the matrix. Rutile grains in the matrix contain relatively little Zr (240–370 ppm).

14

Layered gneiss B94-333 is composed of different layers, which have substantially different garnet compositions and mineralogy. Large, pink garnets from sample B94-333 are characterized by low-Ca contents and core-rim zoning. The garnet cores have some of the highest Mn contents among the studied samples (Alm_{73}, Py_{14}, Grs_{9}, Sps_{5}), the rims have lower Mn and Fe contents but are richer in Ca and Mg (Alm_{56}, Py_{24}, Grs_{18}, Sps_{3}) (Fig. 5, 6). The HREE (Fig. 4, 7) and Y contents decrease from core to rim of the garnet (Yb from 370 to 20 ppm; Y from 1400 to 160 ppm). Zr content of rutile in the matrix and included in garnet is 860–1110 ppm. Orange garnet in another layer has a higher Ca content than the pink garnet and is composed of a large homogeneous core with a thin rim depleted in HREE (Fig. 4, 7). Phengite in the matrix of the sample has lower Si content than inclusions in monazite and zircon (Fig. 5). The TiO_2 content in phengite is about 1.5 wt%, significantly higher than in B01-3. Garnet inclusions in zircon form two separate groups similar in compositions to the two garnet groups from the sample (Fig. 5). Zircon contains coesite inclusions and omphacite with 40% jadeite. Rutile grains in the matrix contain 920–1100 ppm Zr.

Garnet grains in micaschists B94-256 mainly consist of a homogeneous core ($Alm_{61–62}$, $Py_{26–29}$, Grs_{7}, $Sps_{3–4}$) with low concentrations of HREE and Y (120–140 ppm), and have REE patterns with a small negative Eu-anomaly (Eu*/Eu = 0.64–0.47) (Fig. 4, 7). In contrast to the previous two samples discussed, the REE patterns are remarkably constant. Near rims, cracks and inclusions garnet has lower Mg and higher Ca (Alm_{62}, $Py_{21–23}$, $Grs_{10–11}$, $Sps_{3–4}$; Fig.3, 4, 6), HREE and Y, and a more pronounced negative Eu-anomaly (Eu*/Eu = 0.25-0.28). Phengite grains in the matrix are relatively homogeneous and have a high TiO_2 content (Fig. 5). Most phengite inclusions in garnet are very similar to matrix phengite. Phengite inclusions in monazite show a wide range of Si contents (3.1–3.36 Si pfu) with some of the lowest TiO_2 (0.1–0.7 wt%) contents encountered in this study (Fig. 5). Phengite inclusions in zircon have high TiO_2 (2.1 wt.) and Si (3.3 Si pfu) contents, which differ from both the matrix phengite and the inclusions in monazite. Rutile is present only as inclusions in garnet and contains 1030–1050 ppm Zr. Garnet inclusions in zircon have a lower Fe content and higher Ca than the matrix garnet (Alm_{58-60}, Py_{28-31}, Grs_{8-11}, $Sps_{3.3}$; Fig. 5).

Garnet in the diamondiferous gneiss B118A50 is homogeneous in major and trace elements with only slight increase in Mn towards the rim. Garnet inclusions in zircon show a much more variable content in major elements than the matrix garnet (Fig. 5, 6, 7). Phengite in the matrix contains 3.15 Si pfu and 1.5 wt% TiO_2 whereas phengite inclusions in zircon have higher silica (3.2–3.4) and TiO_2 (1.5–3 wt.) content than the matrix mica. Feldspars are represented by almost pure albite and K-feldspar. Large grains of rutile contain less Zr than the previous two samples (790–920 ppm). Inclusions of clinopyroxene in zircon contain 13–57 % of jadeite component and a high Ca-Eskola component, whereas pyroxene is absent in the matrix.

In summary the studied samples present a variety of mineral associations and compositions of matrix and inclusion assemblages. There is a distinct change of garnet zoning in the studied samples. Sample B01-3 shows a pronounced zoning in major and trace elements. Sample B94-333 displays variation of garnet compositions in different layers as well as major and trace element zoning within single grains. This contrasts with the other samples where garnet is largely homogeneous both in major and trace elements with only narrow rims with increase of Mn and HREE (B94-256 and B118A50). This observation suggests that in these two samples, garnet compositions have been equilibrated by either diffusion or recrystallization. This is further supported by the composition of garnet inclusions in zircons that display a much greater variability. Phengite inclusions in monazite and zircon in the majority of samples have higher Si content than phengite in the matrix. Matrix phengite of sample B94-256 has particularly high Ti concentrations, and in sample B01-3 a core-rim increase of Ti and Si-Mg content is observed. Zircon proves to be a robust container of UHP minerals with coesite inclusions in sample B94-256 and B94-333, and diamonds inclusions in B118A50. Relicts of omphacite-rich clinopyroxene were found in the layered gneiss B94-333 and in B118A50. Notably, feldspars are abundant in the matrix of three samples; however they are rare as inclusions in zircon.

Monazite and zircon geochronology

Monazite and zircon are robust minerals and contain inclusions of high/ultrahigh pressure minerals in all the studied samples. Both minerals preserve distinct growth zones. In order to link the ages of domains to metamorphic conditions and coexisting minerals at growth, relevant trace element features are reported. Particular attention is given to Y+HREE as a garnet indicator, Sr and Ba in monazite as possible indicators of feldspar presence, Th/U in zircon as proxy for monazite co-existence (thus high Th/U in magmatic cores), and Ti-in-zircon thermometry.

Monazite from Ky-micaschist B01-3 has a weak core-rim zonation (Fig. 8). Cores usually show a mosaic or polygonal-zoned texture and are brighter in BSE than rims, while the rims have no internal zoning. Monazites have very low HREE contents (Y 100–800 ppm) increasing form core to rim and elevated strontium decreasing from core to rim (Fig. 9). U-Pb analyses yielded $^{206}Pb/^{238}U$ dates between 512±10 Ma and 537±10 Ma. Core and rims analyses return weighted average dates of 529±7 Ma and 525±7 Ma, respectively. With the exclusion of 4 outliers, 24 analyses define a cumulative concordia age of 526±7 Ma (Fig. 10).

Zircons in Ky-micaschist B01-3 have a complex oscillatory-sector internal CL zoning. The trace element patterns of the zircons form two groups corresponding to central and outer parts of the grains (Table S5 and Fig. 11). The outer parts show patterns typical for metamorphic zircons: very low Th content (<10 ppm) and 300–700 ppm U with enrichment in HREE relative to LREE, and a flat but slightly concave pattern for the HREE. The central parts of zircons show anomalous patterns, with a nearly flat REE distribution at 200–5000 times chondrite, strongly enriched in LREE with respect to a typical zircon and rich in HREE, P (up to 4000 ppm), Ti, Y and Th. Analyses with high-LREE patterns have a normal Zr/Si ratios for zircon and SEM investigation did not reveal any inclusion. The rims contain low Ti in the range 2–10 ppm that are in contrast with the elevated Ti concentrations (10–60 ppm) in the domains with high-LREE patterns. The latter have U-Pb dates that scatter from 504±7 Ma to 524±6 Ma and 4 discordant spots. Average $^{206}Pb/^{238}U$ date corrected using the ^{208}Pb method is 515±7 Ma with an high MSWD (4.8) reflecting scatter.

Most monazite grains in layered gneiss B94−333 appear homogeneous in BSE images and a few grains have faint oscillatory zoning in the cores (Fig. 8). Monazites are characterized by a large range of HREE (Y 0.02–1 wt%, Fig. 9), Th (1.7 –11 wt%) and high Sr (0.15–1 wt%). Monazite inclusions in garnet have a higher HREE content (Y 0.35 wt%) than matrix monazite (Y 0.15 wt%). U-Pb dates range between 515±8 Ma and 538±8 Ma with an average $^{206}Pb/^{238}U$ date of 528±7 Ma, MSWD 1.1 (Fig. 10). No correlation between monazite age and composition or texture was observed.

Zircons from layered gneiss B94−333 are of two types according to CL zoning and size (Fig. 12). Small 50-100 μm grains with CL-bright cores and CL-dark rims and large (>200 μm) crystals with dark and mainly structureless CL signal have very thin rims with bright CL. Both populations have Ti concentrations in the same range of 20–52 ppm, low Th/U ratios and a negative Eu anomaly.

Monazite grains in micaschist B94−256 have a patchy zoning that surrounds homogeneous central zones (Fig. 8). Mineral inclusions mostly occur in patchy zoned monazite. $^{206}Pb/^{238}U$ dates range from 510±6 Ma to 533±6 Ma with indistinguishable averages for homogeneous and patchy domains (515±7 and 523±5 Ma, respectively, Fig. 10). All analyses define a concordia age of 521±6 Ma (MSWD 1.5).

In sample B94-256 zircon crystals have consistently CL-dark cores and CL-bright rims (Fig. 2). Cores have slightly lower REE contents than rims with the exception of one core with an unusually high LREE content (Fig. 11). Ti concentrations range from 12–84 ppm in the cores to 100–150 ppm in the rims. $^{206}Pb/^{238}U$ dates (^{204}Pb corrected) span from 516±9 to 530±8 Ma (Fig. 10), with the exception of one core with high LREE and Th/U that yield a $^{207}Pb/^{206}Pb$ date of 2867±70 Ma. The average age is 522± 6 Ma (MSWD 0.6, N 14) with no appreciable difference in age between cores and rim.

Zircons from diamondiferous gneiss B118A50 show concentric zoning with CL-dark cores, mantles with variable CL intensity and CL-dark rims. The cores have low Th/U ratios <0.05 and 9–63 ppm Ti. These cores are overgrown by CL-bright mantles that have higher Ti (46–108 ppm) and Th/U ratio (0.04–0.3). CL-dark rims have Ti contents of 32–64 ppm similar to the cores, but with higher Th/U ratios (0.05–0.15). Zircon REE patterns show little variation with a flat distribution of HREE, a small negative Eu anomaly and a large positive Ce anomaly. Most U-Pb analyses yielded dates from 503±7 Ma to 532±7 Ma with an average of 520±7 Ma, but with a high

MSWD of 4.3 reflecting scatter above analytical uncertainty. However, U-Pb dates of cores, mantles and rims are overlapping and indistinguishable within the precision of measurements (Fig. 10c).

Discussion

The studied samples have large variations of mineral assemblages in matrix and inclusions, as well as different mineral compositions. It is necessary to first establish to what extent these differences are related to variable metamorphic conditions in the context of possible diffusion equilibration in minerals during UHP metamorphism. By correlating the growth of monazite and zircon to metamorphic minerals it is then possible to evaluate whether all rocks were metamorphosed during the same subduction-exhumation event and to discuss tectonic implications.

Constraints on peak metamorphic conditions

Determination of peak metamorphic temperatures in UHP rocks is challenging for several reasons. Retrograde reactions can eliminate peak assemblages and P-T determination in such rocks hinges on minerals that survive decompression from UHP conditions. Additionally, if decompression occurs at high temperature, many UHP rocks undergo phengite melting during exhumation (Hermann and Rubatto 2014). Thus the best chance to preserve UHP conditions is in rocks with relatively low peak metamorphic conditions that experienced significant cooling during exhumation. The diamondiferous gneisses from Kokchetav massif have experienced extensive melting as well as a granulite facies overprint (Sobolev and Shatsky 1990; Hermann et al. 2001; Stepanov et al. 2014). In such rocks only a few minerals like garnet, kyanite, zircon and rutile might survive from UHP conditions. An additional problem is that at high temperatures, diffusion equilibration can modify major and trace element compositions of peak minerals and thus

20

eliminating the information about the prograde and peak conditions. In our attempt to reconstruct the metamorphic histories of the four samples we first focus on Ti-in-zircon and Zr-in-rutile thermometry because these are systems with slow diffusion, even at extreme temperatures (Ewing et al. 2013). Then we discuss the information obtained from inclusions before addressing P-T estimates using the main minerals garnet and phengite.

Ti-in-zircon thermometry. Application of the Ti-in-zircon thermometer shows that different samples achieved different peak temperatures. In the diamondiferous gneiss B118A50, zircons mantle zones with diamond inclusions record Ti-in-zircon temperatures (Ferry and Watson 2007) of 910–1040°C (Fig. 13), corroborating peak conditions of UHP metamorphism of 950–1000°C at >45 kbar (e.g. Sobolev and Shatsky 1990; Hermann et al. 2001). Rim zones of zircon from B94-256 yield Ti-in-zircon temperatures of 960–1080°C, suggesting similar peak metamorphic conditions. Samples B01-3 and B94-333 yield markedly lower maximum Ti-in-zircon temperatures (645–720 and 815–940°C, respectively) indicating lower peak temperatures for these samples.

The Ti-in-zircon thermometer (Ferry and Watson 2007) was calibrated for pressures close to 10 kbar. Tailby et al. (2011) proposed that at high pressure the Ti-in-zircon thermometer underestimates temperature; however Ti-in-zircon temperature estimates for the diamond bearing gneisses B118A50 are close to peak T estimates at 950–1000°C by other methods (e.g. Sobolev and Shatsky 1990; Hermann et al. 2001). Additionally Ferriss et al. (2008) suggested, that with increasing pressure Ti might change the preferred site from substituting Si to substituting Zr and therefore increase of pressure might increase the solubility of Ti in zircon. Considering these uncertainties, Ti-in-zircon temperatures are used in a relative sense: similar temperatures are considered representing similar PT conditions although absolute values may be somewhat inaccurate.

Zr-in-rutile thermometry. The investigated samples show a large range in concentrations of Zr in rutile: 240–370 ppm in matrix rutile in micaschist B01-3, 860–1100 ppm in rutile inclusions and matrix grains in layered gneiss B94-333, 1030–1050 Zr ppm in rutile inclusions in B94-256 and 790–920 Zr ppm in large rutile grain in garnet gneiss B118A50 (Table S8). For sample B01-3 Zr in rutile thermometer for the α-quartz field using the calibration of Tomkins et al. (2007) provides temperatures of 670–710°C. For the Zr range observed in samples B94-333, B94-256 and B118A50, the Tomkins et al. (2007) calibration predicts 820–860°C, which are temperatures substantially lower than other estimates. Indeed Tomkins et al. (2007) expressed concern with their calibration at high pressures and suggested that a correction of up to 100°C might be needed at 40 kbar. The four experiments at 30 kbar conducted by Tomkins at al. (2007) define a regression described by the following equation:

$$T(°C)=14703/(-Ln(Zr\_ppm)+ 18.909)-273$$

This calibration indeed gives 100°C higher temperatures than Tomkins et al. (2007) proposed for conditions in the coesite field. For sample B94-333 this calibrations gives 930–960°C. Considering that at pressures of 45–50 kbar the proposed pressure correction on the thermometer might be even higher, we conclude that rutile compositions in samples B94-256 and B118A50 is consistent with formation of rutile at peak temperatures of 1000°C. Therefore, similar Zr concentrations in rutile in sample B94-33, B94-256 and B118A50 are likely affected by the same pressure effect on the thermometer. Studies of eclogites from the Dabie orogen demonstrated that the Zr-in-rutile thermometer commonly underestimates temperatures for peak conditions (Zheng et al. 2011). The

22

high pressure calibration of Zr-in-rutile thermometer obtained in this study is particularly suitable for Dabie-Sulu where maximum pressure was very close to 30 kbar. For Dabie rutile with 45–130 ppm Zr (Zheng et al. 2011) the new calibration gives 700–770°C which are close to estimates from other geothermometers (Zheng et al. 2011). For rutiles from the Sulu UHP rocks with 100–340 ppm Zr temperature estimates of 750–850°C are also consistent with data from conventional thermobarometry. Therefore, we conclude that a pressure correction for the application of the Zr-in-rutile thermometer to UHP samples is necessary.

Inclusions in zircon and monazite. Numerous studies have demonstrated that zircon is an exceptionally robust host mineral for HP/UHP inclusions because it recrystallizes at these conditions, does not react with other silicates, and has a robust crystal structure (Sobolev et al. 1991; Vavilov et al. 1993; Korsakov et al. 1998, 2002; Katayama et al. 2000; Hermann et al. 2001; Liu et al. 2001, 2002). The capacity of monazite for preservation of HP-UHP minerals is less known though there are reports of diamond inclusion in monazite from quartzo-feldspathic rocks from the Erzgebirge (Massonne et al. 2007). Monazite is a potentially robust host for inclusions, because as a REE phosphate, it has limited ability for cation exchange with silicate minerals. Zircon and monazite from the studied samples contain inclusions of phengite, garnet, clinopyroxene, rutile and a SiO_2 phase. The composition of these inclusions serves to reconstruct the conditions at which they have been trapped.

Raman spectroscopy confirmed that zircon from sample B118A50 contains coesite and diamond inclusions, which are typical for these UHP gneisses. Inclusions of coesite in zircon were identified in samples B94-256 and B94-333, commonly with partial transformation to quartz. These observations provide unequivocal evidence that these three samples experienced UHP conditions. No coesite has been identified in sample B01-3. A systematic study of SiO_2 inclusions in garnet has shown that only quartz is present and has not given any hint for precursor coesite. Some inclusions of quartz display a shift in Raman peaks, indicating that the quartz inclusions retain an internal pressure of ≈10 kbar (Korsakov et al. 2009).

Phengite composition as indicator of metamorphic conditions. Experimental studies on the composition of phengite in subducted sediments have shown that the Si content increases strongly with P and decreases with T whereas TiO_2 increases strongly with increasing T and decreases slightly with increasing P (Hermann 2002; Auzanneau et al. 2010). Phengite is present in all samples either as matrix mineral and/or as inclusion, providing an excellent framework to test to what extent phengite is able to retain P-T information. Phengite inclusions in zircon from micaschist B94-256 have high Ti and Si contents (Fig. 5) comparable with mica from UHP sample B118A50 as well as micas produced in experiments at 35–45 kbar and 900–1000°C (Hermann and Spandler 2008; Auzanneau et al. 2010) demonstrating that these two samples attained higher peak conditions than other samples. Matrix phengite in sample B94-256 has a lower Si content than the inclusions in zircon (Fig. 5) indicating equilibration of matrix phengite during exhumation. The high TiO_2 content in the matrix mica suggests that this equilibration took place still at high P-T conditions. In contrast in sample B118A50 matrix phengite shows much lower Si and Ti concentrations and thus is likely a late, retrograde phase. Phengite inclusions in monazite from micaschist B94-256 have low Ti contents and show a large range of Si contents similar to phengite from B01-3. This observation is best explained by the formation of the phengite inclusions during the prograde path. Phengite inclusions in monazite and zircon from sample B94-333 have generally lower maximum Ti and Si contents than zircon inclusions in sample B118A50, thus suggesting overall lower metamorphic conditions. Mica inclusions in sample B01-3 have comparable maximum Si content but lower Ti content than sample B94-333, indicating that B01-3 formed at lower temperatures. Considering the positive slope of lines of constant Si content of mica in P-T space, sample B01-3 thus records the lowest P-T among the studied samples.

Metamorphic PT paths

We have shown that the there is clear evidence for different metamorphic conditions in the four studied samples and that we were able to obtain garnet and phengite compositions for all samples. In this section we will apply garnet-phengite-kyanite and garnet-phengite-omphacite barometry (Ravna and Terry, 2004) in conjunction with independently determined temperatures to constrain the peak conditions of the samples. The coherent use of the Ravna and Terry (2004) calibration is especially useful to highlight relative differences between the investigated samples. The set of thermobarometers are applied to matrix and inclusion assemblages. Matrix assemblages have the advantage that textural equilibrium can be observed in thin section but the disadvantage that mineral compositions might be modified during retrograde processes. Inclusion assemblages preserve the composition from the time of trapping but it is more difficult to establish that these inclusions were co-existing. We will use only P-T estimates from mineral inclusions that derive from a single zircon domain (for which we can also obtain a Ti-in-zircon temperature) to minimize these problems.

Kyanite-micaschist B01-3 preserves strong zonation in major and trace elements in garnet, shows low Ti-in-zircon temperatures and has no evidences of UHP conditions. Therefore we conclude that this sample attained the lowest PT conditions among the studied samples. Three P-T estimates were obtained corresponding to garnet cores, mantles and rims.

Garnet cores host inclusions of xenotime and quartz and contain 1200–1400 ppm Y corresponding to a temperature of 510±10°C (Pyle and Spear, 2000). Phengite-garnet Fe-Mg exchange geothermometer (Green and Hellman, 1982; low Ca, low Mg) also yields a temperature of 500°C. From the low-Si phengite inclusions in monazite a pressure of 11±2 kbar is estimated by the Grt-Phe-Ky barometer (Ravna and Terry, 2004). Garnet mantles also contain xenotime and lower Y (600–400 ppm), which gives temperatures of 550±10°C (Pyle and Spear, 2000) in good agreement with 570°C obtained from Fe-Mg exchange between garnet mantle and included phengite using the calibration of Green and Hellman (1982; low Ca, low Mg). Grt-Phe-Ky barometry of this assemblage (Ravna and Terry, 2004) yields 23±2 kbar.

Garnet rims display the highest Ca and Mg contents and thus likely formed at peak metamorphic conditions. The decrease in Eu anomaly from the garnet mantle to the rim might indicate disappearance of feldspar from the main assemblage. Zircons contain 2–10 ppm Ti, which corresponds to temperatures of 640–730°C (Ferry and Watson, 2007). The sinusoidal shape of the HREE pattern of zircons resembles that of the garnet rims, thus providing evidence that the zircons crystallized together with the garnet rims. In the matrix, phengite crystals from core to rim show a decrease in Mg (which serves as an indicator for the celadonite component in phengite) and an increase in TiO_2 contents (Fig. 3a–d) indicting an increase in temperature. Rutile in the matrix contains 240–370 ppm Zr with an average of 300 ppm. Simultaneous application of the Grt-Phe-Ky barometer (Ravna and Terry, 2004) with the Zr-in-rutile thermometer (Tomkins et al, 2007) yields a temperature of 690–730°C and pressure of 24±2 kbar. Application to the same compositions of Fe-Mg exchange geothermometer (Green and Hellman, 1982; low Ca, low Mg) provided temperature estimate of 780°C. These are the highest PT conditions recorded by samples B01-3 and thus represent peak metamorphism (Fig. 14a).

The layered gneiss B94-333 clearly attained conditions of UHP metamorphism as documented by the presence of coesite and omphacite inclusions in zircon. The absence of omphacite in the matrix association and also different compositions of phengite inclusions and matrix phengite indicate that the matrix phengite reequilibrated during retrogression. The pressure sensitive Grt-Phe-Ky equilibrium applied to matrix phengite and garnet rim, combined with Zr-in-rutile thermometry yields conditions of 800±30°C and 20±2 kbar. Even lower pressures are obtained for matrix mineral assemblages involving plagioclase. The Grt-Phe thermometer (Green and Hellman, 1982) for the composition of matrix phengite and low-Ca garnet rims gives a temperature estimate of 740±30°C. Application of the Grt-Pl-Ms-Qtz geobarometer (Hodges and Crowley, 1985) to such a matrix assemblage and the low-Ca garnet gives pressure estimates of 12±3 kbar. Peak conditions might be retrieved by applying thermobarometry to the Grt-Phe-Cpx inclusion assemblage hosted in zircon: zircon temperatures range from 800–900°C and calculated pressures are 29±2 kbar, just within the coesite stability field.

Important features for the diamondiferous gneiss B118A50 include: (1) homogeneous garnet due to diffusional re-equilibration of major and trace elements (Fig. 3, 4, see also discussion below), (2) high Ti-in-zircon temperatures up to 1040°C (Fig. 13), (3) diamond, coesite and high-Si and high-Ti phengite inclusions in zircon, (4) significant depletion of LREE, Th and U in bulk rock, which is evidence of high temperature melting and melt loss (Stepanov et al. 2014). Using a peak temperature of 1000°C, as constrained by the Ti-in-zircon thermometry of the domain that hosts the inclusions, peak pressures of 49±4 kbar are calculated using the Grt-Phe-Cpx equilibrium applied to garnet with maximum Mg content, omphacite with maximum Na content and phengite with maximum Si content (Ravna and Terry 2004). Without constraining the temperature first and using the solver function peak conditions of 47±5 kbar and 930±45°C are obtained.

Similarly to other UHP gneisses, sample B118A50 was intensely retrogressed as no omphacite is preserved in the matrix and garnet and phengite are partly replaced by secondary biotite or chlorite. Using matrix phengite and unzoned garnet compositions, much lower metamorphic conditions of about 18 kbar and 700°C are obtained. We conclude that that sample B118A50 experienced partial melting and melt loss at UHP conditions and peak conditions as well as a PT path similar to other UHP samples from Kokchetav investigated in previous studies (Sobolev and Shatsky 1990; Hermann et al. 2001; Chopin 2003): peak at 950–1000°C and >45 kbar, and exhumation through 800°C and 10 kbar, 550–600°C and 5 kbar (Fig. 14).

Micaschist B94-256 has high Ti-in-zircon temperatures (up to 1080°C, Fig. 13), contains coesite and high Ti and Si content in phengite inclusions in zircon (Fig. 5), and almost completely homogenous garnet due to diffusional homogenization. All these features of sample B94-256 are comparable to sample B118A50, thus we propose that it reached similar peak conditions. Using the composition of garnet and phengite inclusions in the high temperature zircon domain, a pressure of 49 kbar is calculated at 1000°C assuming that kyanite was present at peak UHP conditions (if not, this would represent a minimum pressure). Contrary to other UHP gneisses, sample B94-256 still has large amounts of phengite preserved and shows no signs of partial melting. It has a more homogeneous texture than the typical UHP gneisses (Stepanov et al, 2014) and its bulk rock composition is not depleted in LREE, Th, U, which are highly depleted in the typical UHP gneisses (Stepanov et al, 2014).

28

Presence of melt is considered as a main factor for the poor preservation of UHP assemblages in the Kokchetav gneisses (Hermann et al, 2001). Preservation of high-Ti phengite in the matrix of sample B94-256 provides evidence for subsolidus equilibration during exhumation possibly due to combination of low water activity and temperature below the phengite melting curve. The Grt-Phe thermometer for garnet rims and matrix phengite (Green and Hellman, 1982, low Ca, low Mg) gives temperatures of 700±20°C for the matrix association. The Grt-Phe geobarometer of Ravna and Terry (2004) for this assemblage gives a pressure estimate of 21±2 kbar (Fig. 14), which is substantially higher for an equivalent temperature than the estimated PT path for the typical UHP gneiss B118A50. Biotite was formed by replacement of garnet and this reaction could have produced an increase of HREE contents in cracks and garnet rim (Fig. 4c, 7). The increase in Eu anomaly in garnet rims might indicate formation of plagioclase during this stage.

Monazite in micaschist B94-256 contains inclusions of K-feldspar and phengite with Ti contents much lower than matrix phengite and a wide variation in Si content (3.15–3.35 pfu). As Ti in phengite is strongly temperature dependent (Hermann and Spandler, 2008; Auzanneau et al, 2010), it suggests that the monazite and its inclusions formed at a lower temperature stage than peak conditions (e.g. the prograde PT path).

Homogeneization of garnet composition with increasing metamorphism and implications for Sm-Nd and Lu-Hf dating

Previous studies of UHP rocks from Kumdy-Kol and Barchi-Kol demonstrated that commonly garnets are homogeneous in major elements (Sobolev and Shatsky 1990; Korsakov et al. 2002; Massonne 2003) or record retrograde zonation with decrease of MgO and CaO accompanied by increase of MnO (Korsakov et al. 2002) and may have zoning in oxygen isotopes (Sobolev et al. 2011). We report for the first time zonation of Kokchetav garnets from the UHP terrain for various trace and minor elements, most importantly Mn, HREE and Y. Because garnet has a high affinity for Mn, HREE and Y it controls the budget of these elements and thus zonation in these elements may record changes in the modal abundance of garnet in the rock. The first garnet that forms during prograde metamorphism will have a high Mn content and its HREE and Y content are controlled by equilibrium between garnet and monazite and xenotime (Yang and Pattison 2006; Spear and Pyle 2010). With increasing P-T, the fraction of garnet in the rock increases and garnet becomes the main host for HREE, Y and Mn (Yang and Pattison 2006; Konrad-Schmolke et al. 2008; Spear and Pyle 2010) with a progressive decrease in the abundance of these elements in garnet (so called Rayleigh fractionation). Because diffusion of REE in garnet is significantly slower than of major elements (Van Orman et al. 2002; Tirone et al. 2005; Carlson 2012), REE zoning will persist at significantly higher temperature than major elements zoning (Hermann and Rubatto 2003).

The studied samples show remarkably different types of garnet zoning in major and trace elements (Fig. 3–5). Garnets in samples B118A50 and B94-256, which underwent the highest metamorphic grade, are essentially homogeneous, with a slight increase of HREE and Mn in cracks and rims. This zoning can be explained by complete homogenization of garnet during peak conditions both in major and trace elements and slight garnet dissolution during retrogression. Contrastingly, in samples B94-333 and B01-3 garnets have cores rich in HREE and Y, which decrease toward the rims by orders of magnitude. Sample B01-3 also preserves high concentrations of Mn in the core. In summary, the type of garnet zoning is related to metamorphic temperature: samples B118A50 and B94-256 achieved the highest temperatures, above the closure temperature for REE diffusion in garnet; sample B94-333 achieved conditions above the closure temperature for major divalent cations, but insufficient for REE diffusion. The temperature in sample B01-3 was not high enough even to homogenize major elements.

This information can be combined with the peak P-T estimates of the samples. Homogenisation of major element is not achieved at 710°C for a maximum duration of 5–10 Ma (see next section). REE diffusion is not observed in B94-333 reaching 850–900°C. These data are in agreement with obliteration of major element zonation and preservation of intensive REE zonation in 1 cm garnets from Val Malenco which experienced metamorphism at 700–850°C over 40 Ma (Hermann and Rubatto 2003). Diffusion modeling in garnet predicts that for geological timescales diffusion starts to affect major elements at temperatures above 600°C and above 750–800°C major element zoning in mm-sized garnet is homogenized in a few million years (Caddick et al. 2010). This is consistent with observations of essentially homogeneous garnets in granulites from the Bohemian Massif, which experienced peak metamorphic temperatures of at least 900°C (Kotková and Harley 2010). REE equilibration by diffusion or recrystallization is complete in samples B118A50 and B94-256 with peak temperatures of 950–1000°C. Thus, for a metamorphic duration of 5–10 My, REE diffusion equilibration is likely taking place at about 900–950°C.

The homogenization of REE by diffusion can significantly affect Sm-Nd and Lu-Hf geochronology (Anczkiewicz et al. 2007). In rocks with garnet preserving REE zonation, early formed garnet cores are characterized by high Lu content and Sm/Nd ratios, therefore such cores record the time of prograde metamorphism (e. g. Anczkiewicz et al. 2007). In high temperature rocks homogenization of REE would result in elimination of prograde zoning and hence Sm-Nd and Lu-Hf isotopic systems would record the time of peak metamorphism. Our data on

31

homogenization of garnet REE zonation at 900–950°C are in agreement on estimates of closure of Lu-Hf system below 900°C by Anczkiewicz et al. (2007).

Timing of subduction and exhumation of the Barchi-Kol terrain

Inclusion assemblages in zircon and monazite and trace elements, particularly REE, allow to link different domains in these minerals to metamorphic events.

In HP Ky-micaschist B01-3 monazite has a very low HREE content increasing from core to rim, which can be explained by an increase of $D^{mnz/grt}$ with temperature as proposed by Pyle et al. (2001). Monazite contains an inclusion assemblage (Grt, Phe, Ky, Rt and Qtz) identical to that of the matrix and the compositions of garnet and phengite inclusions in monazites are also identical to those of garnet rims and matrix phengite, respectively (Fig. 5). These observations indicate that the growth of monazite at 526±7 Ma was contemporaneous with garnet rims that formed at peak temperatures. Zircons have domains with "normal", LREE depleted and "anomalous", high-LREE patterns. Zircons with "normal" patterns have sinusoidal REE patterns with small depressions in Ho, Er, Tm relative to Tb, Dy, Yb, Lu. This feature can be explained only by zircon equilibrium with garnet rims, which also show a concave REE pattern (Fig. 4, 11). Zircons with "anomalous" REE patterns show enrichment in HREE, LREE, Th, Ti and P. These analyses correspond to core domains as observed in optical images (Fig. 1212), which are interpreted as inherited cores. Ages of the LREE zircon domains scatter in the range 504–524±7 suggesting growth over time from metamorphic peak to retrogression.

In layered gneiss B94-333 monazite shows significant variation in HREE content and monazite inclusion in garnet has higher HREE concentrations than matrix grains. This HREE variation is reflected in the garnet zoning from core to rim linking the growth of the two minerals during the prograde to peak path. High Sr contents in monazite indicate that it crystallized at pressures exceeding the stability field of feldspar (Finger and Krenn, 2007). During the decompression monazite became unstable and was replaced by an assemblage of apatite, synchysite and Th-bearing minerals (Stepanov et al, 2014). As grains with different zoning and trace element composition show no systematic age difference we concluded that the prograde to peak path occurred within the time interval of 528±7 Ma. The variation in composition of garnet inclusions, CL structures, and trace element composition of zircon indicate that zircons were formed from two distinct bulk compositions in this banded sample. Ti-in-zircon temperatures are very close in both populations, thus indicating similar peak conditions. Zircons have REE patterns with low HREE concentrations and small Eu anomalies, indicating formation at high pressure conditions in the presence of garnet and absence of feldspar (Rubatto 2002). Garnet inclusions in such zircons are similar in composition to the mantles of low-Ca garnets, indicating their simultaneous formation. Zircon from this sample was not dated.

In UHP micaschist B94-256 monazite with homogeneous BSE and high HREE is overgrown by patchy monazite with lower HREE, both with prograde phengite inclusions. The decrease of HREE content from the early to later generation can be explained by growth of monazite on the prograde path in equilibrium with garnet, which progressively extracted HREE. Unrealistically high $D_{Lu}^{mnz/grt}$ of 50 between monazite and garnet ($D_{Lu}^{mnz/grt}$=2–3 reported for granulites, see Rubatto et al. 2006) also indicates that the garnet currently present in the rock did not form in equilibrium with monazite. The observed variation in monazite provides evidence that REE were not homogenized by diffusion even at high temperatures of 1000°C. Homogeneous monazite domains

33

yield an age of 515±7 Ma and patchy zones are 523±4 Ma, which are identical within the precision of the measurements. Given the high temperature of equilibration, it is not clear whether monazite dates prograde metamorphism or whether the pooled age of 521±8 Ma represents a cooling age.

Zircons in micaschist B94-256 have two major growth zones: a core and a rim. From core to rim, HREE and Ti contents increase. Inclusions in both domains of zircon correspond to a high pressure association of garnet, phengite and rutile. The REE patterns lack a negative Eu anomaly (Fig.11) consistent with their HP origin. One zircon core yield an inherited $^{206}Pb/^{207}Pb$ age of 2867±72 Ma. This grain also has rising REE pattern and a high Th/U ratio of 0.14 typical for igneous zircon (Fig. 11). All other zircons show very low Th/U (0.03–0.006), presumably because Th was hosted by coexisting monazite (Stepanov et al. 2012). The low Th/U ratios of zircon from sample B94-256 differ markedly from samples B118A50 and B94-333 which contained melt at some stage of the evolution and both samples contain zircon with zones of high Th/U ratios, which suggests monazite dissolution in the melt. Zircon cores and rims do not have any systematic difference in age (cores: 522±6 Ma, and rims: 522±7 Ma). Given that in this sample an inherited core was found, complete resetting of Pb seems unlikely and the obtained ages are interpreted to date conditions close to the UHP peak metamorphism.

In diamond-bearing gneiss B118A50 zircon cores have low Th/U ratios, and grew on the prograde part of the PT path, when Th was hosted by monazite. Mantles have highest Ti-in-zircon temperatures and high Th/U ratios, indicating their growth at peak conditions, when monazite was dissolved in the melt. The decrease of Ti-in-zircon temperatures indicates formation of rims during exhumation. SHRIMP dating of zircons from B118A50 resulted in scatter of dates from 503±7 to 532±7 Ma (Fig. 10). However this scatter does not correlate with zircon's texture or composition.

This observation suggests that the Pb in zircon might have been at least partially reset during peak temperatures of 1000°C.

While previous geochronological studies mostly investigated zircons from diamondiferous UHP rocks of the Kokchetav complex (Claoue-Long et al. 1991; Hermann et al. 2001; Katayama et al. 2001; Ragozin et al. 2009), we obtained new U-Pb ages from monazite and zircons from samples with different P-T paths including UHP and non-UHP samples from the Barchi-Kol unit (Fig. 15). Monazite ages from samples that did not reach UHP conditions constrains HP metamorphism at 528±8 for Ky-micaschists B01-3, and 528±7 Ma for layered gneiss B94-333. As the peak metamorphic conditions of these rocks are well below the closure temperature for Pb diffusion in zircon and monazite (Lee† et al. 1997; Cherniak et al. 2004), the obtained ages are interpreted as formation ages. Different zircon domains in the UHP gneiss B118A50 vary in age from 503±7 to 532±6 Ma and UHP micaschists B94-256 monazite and zircon give ages at 521±13 Ma and 522±6 Ma, respectively. Both rocks reached peak metamorphic conditions of 1000°C and it is not clear if the obtained ages are affected by diffusional Pb loss. There has been some evidence for partial lead loss in zircons from diamondiferous gneisses in the study of Hermann et al. (2001). They observed zircon cores with low-pressure inclusions and trace element patterns typical for inherited detrital cores that gave an age indistinguishable from the age of UHP metamorphism. The combined data set from this study and Hermann et al. (2001) thus shows that zircon and monazite are able to retain trace element characteristics up to at least 1000°C, whereas it seems likely that at least partial loss of Pb occurred at these extreme conditions. This uncertainty highlights the value of having ages of rocks in the same suite that experienced lower grade metamorphic conditions, where diffusional Pb-loss is not relevant. The obtained ages in this study are consistent with

35

previous ages of UHP metamorphism and exhumation in the Barchi-Kol UHP terrain obtained by U-Pb dating at 528±5 Ma (Hermann et al. 2001), and in the Kumdy-Kol terrain at 519±8 Ma (Katayama et al. 2001), 526±5 (Ragozin et al. 2009) and Sm-Nd dating at 524–535 Ma (Shatsky et al. 1999, p. 199) (Fig. 15). Our results confirm that peak metamorphism and exhumation occurred over a relatively short period of time and provide additional evidence that prograde metamorphism also occurred during the same time interval.

Assembly of slices with different PT paths

This study documents the occurrence of rocks with different P-T paths and peak metamorphic conditions within the restricted area of the Barchi-Kol UHP terrain (Fig.1). All samples display indistinguishable ages and thus belong to the same overall subduction and exhumation cycle. Three potential scenarios could explain how rocks with an apparently different evolution can be closely inter-layered: All samples experience UHP conditions, but some (1) did not react to form UHP minerals, or (2) were completely retrogressed upon exhumation. (3) Alternatively, the different rock types are part of a tectonic mélange that assembled small UHP and non-UHP slices during the subduction-exhumation cycle.

The feasibility of the first scenario is demonstrated by the presence of metagabbros that were not completely transformed into eclogite within the HP units of the Western Gneiss Region and Zambia (Engvik et al. 2001; John and Schenk 2003). In such cases, transformation of gabbro to eclogite was controlled by the presence of hydrous fluid, and dry gabbros preserved their protolith texture and composition. Another example are quartz-feldspatic gneisses in the Western Gneiss Region where feldspars survived at UHP conditions (Peterman et al. 2009). This scenario is not applicable to the Kokchetav rocks as they all have a gneissic/schistose texture and contain hydrous minerals. In these samples deformation and the presence of fluid/melt would have facilitated re-equilibration (Holloway and Wood 1988). Additionally, all samples display prograde metamorphic features as well as the same metamorphic age.

The second scenario is common in many UHP gneisses and eclogites of the Kokchetav, Dabie-Sulu, and Western Gneiss Region where evidence of UHP conditions is completely obliterated in rock-forming minerals. Rocks that mostly preserve UHP rock-forming minerals are very rare (the most notable examples are calc-silicate rocks and marbles from the Kokchetav and whiteschists from Kokchetav and Dora Maira). Typically the only evidence left of UHP metamorphism are inclusions in robust minerals such as zircons and maybe garnet (Sobolev et al. 1994; Carswell et al. 1999; Liu et al. 2002). This scenario is valid for the diamond-bearing gneiss B118A50, but the other three samples do not show this extensive retrogression and preserve prograde and peak metamorphic features. The combined investigation of garnet, phengite and mineral inclusions compositions, coupled with garnet and zircon trace element zoning demonstrates that the four samples experienced different P-T trajectories. Therefore we conclude that, for the samples investigated in this study, the most likely scenario is the assembly of rocks with different P-T path during the subduction-exhumation cycle of the Kokchetav continental margin.

Implications to thermal structure of subduction zone

Previous models proposed that the entire Kokchetav UHP unit underwent a common metamorphic history (Kaneko et al. 2000; Liou et al. 2002). There is indeed ample evidence that

37

many Kokchetav rocks experienced a similar UHP P-T paths based on (1) abundance of metamorphic diamonds in gneisses, marbles, and calc-silicate rocks; (2) diamonds with a similar range of nitrogen aggregation state (Cartigny et al. 2001; Nadolinny et al. 2006; Sitnikova and Shatsky 2009); and (3) comparable trace element composition in the majority of UHP gneisses, which is consistent with partial melting and melt extraction at similar PT conditions (Stepanov et al. 2014). However in this study we report evidence that other rock types within the same unit (collected within 10 m to 1 km from the typical UHP rocks) underwent different PT paths. To explain this complexity, we suggest that rocks with different P-T trajectories were assembled by sampling different, but proximal parts of the subducted slab during exhumation. Because of the very similar age of metamorphism in all samples, the different P-T conditions recorded allow insights into the thermal structure of the subducted continental crust at different depths. This provides an excellent opportunity to compare the obtained P-T trajectories with theoretical thermal models of subducted crust.

The initial part of the PT path in sample B01-3 is along a low temperature gradient, typical of subduction tectonics. This is followed by an almost isobaric increase of temperature at about 24 kbar, corresponding to about 80 km depth. Kinked P-T paths during subduction have been predicted by several independent geodynamic models of subduction zones (van Keken et al. 2002; Syracuse et al. 2010; Gerya 2011). The increase in temperature is related to the coupling of the subducted slab with the mantle wedge. At the transition from partial to full coupling the hot mantle wedge is getting much closer to the subducted slab, resulting in a temperature increase of 200–300°C, over a very small pressure increase (Syracuse 2010). Typically, this transition is expected at a depth of 60–100 km in oceanic subduction zones, depending on the thermal structure

38

of the lithosphere in the hanging wall of the subduction zone. In continental collision zones, the coupling depth is not well constrained and the effect of hot mantle might be more subtle resulting in a temperature increases over a larger pressure range (Warren et al. 2008; Gerya 2011). In any case, the temperature structure of the hanging wall will impact on the pressure-temperature path of the subducted crust. In the Barchi-Kol samples, we observe a heating with limited pressure increase at about 22 kbar, indicating a relatively thin lithosphere in the hanging wall of the subduction. Other classical UHP terrains such as the Dora-Maira Massif in the Western Alps do not show any evidence for such a heating event and peak metamorphic temperatures are considerably lower at 40 kbar, 730°C (Hermann, 2003). Therefore, this would be consistent with a thicker lithosphere above the subducted crust, where the coupling between the slab and the mantle wedge occurred at a depth exceeding 100 km. The geodynamic models predict that once the subducted rocks are coupled to the mantle wedge, the temperature increases only moderately with increasing pressure. Models typically show a gradient of 5–7°C per kbar. This is again consistent with the reconstructed P-T path of the higher grade rocks where a temperature increase of about 250–300° is documented for the increase of pressure from 22–50 kbar. Therefore the combined prograde PT path obtained for Barchi-Kol terrain is in good agreement with predictions of numerical geodynamic models for subduction zones.

The presence in the Barchi-Kol unit of UHP rocks that experienced melting (diamondiferous gneiss B118A50) and others that did not (micaschist B94-256) is also intriguing. We attribute this to their distribution within a subduction channel where large T gradients are present between the subduction cold oceanic lithosphere and the hot (above 1200°C) mantle wedge, as shown in recent models (van Keken et al. 2002). The fast subduction-exhumation cycle would have also favored the

39

preservation of large temperature gradients in the terrain because dissipation of a temperature gradient is a time dependent process.

Conclusions

Our detailed petrographic and geochronological investigation of metasedimentary rocks from the Barchi-Kol UHP area in the Kokchetav complex demonstrates that the rocks experienced different peak pressures ranging from 25–50 kbar and peak temperatures from 700–1000°C, as well as variable cooling paths on exhumation. Timing of metamorphism in the investigated samples (521–528 Ma) was similar to the metamorphism of other Kokchetav UHP rocks, demonstrating that deep subduction, peak metamorphism and exhumation occurred over a relatively short period of time. The contrasting P-T conditions of the samples can be used to constrain the thermal structure of the subducted continental margin at 530–520 Ma. Two samples provide evidences for a 200°C temperature increase at a pressure of ~25 kbar, in agreement with thermal models of subduction zones where such a temperature increase occurs at the transition from partial to complete coupling of the downgoing plate with the mantle wedge.

Our study demonstrates the importance of accessory minerals not only for geochronology but also for reconstruction of the PT path of the HP/UHP rocks. In major minerals, information about the prograde evolution and peak conditions is limited to trace element zoning in garnet. In accessory minerals, trace element compositions and inclusions provide a much more detailed record and may be the only evidence of the prograde evolution and peak conditions. We also document how garnet trace element zoning can be used for the discrimination of HP/UHP rocks with different histories. The combination of garnet trace element zoning with trace element geochemistry of resistant accessory minerals produces a detailed picture of subduction metamorphism.

The main finding of this study is that UHP terrains have a more complicated internal structure than what it is usually thought. Within the UHP block of the Kokchetav complex rocks with completely different metamorphic histories are associated at the 10 meter scale.

Deposit Items

Tables with major and trace element compositions of minerals, results of U-Pb dating, and diagrams with sequences of mineral evolution are presented in the electronic deposit items.

Acknowledgements

We thank Terry Mernagh for analytical assistance and Carl Spandler for valuable suggestions, comments and corrections. AVK thanks Russian Science Foundation (RSF 15-17-30012). The reviews of Vladislav Shatsky and an anonymous reviewer helped to improve the manuscript.

References

Anczkiewicz, R., Szczepański, J., Mazur, S., Storey, C., Crowley, Q., Villa, I.M., Thirlwall, M.F., and Jeffries, T.E. (2007) Lu–Hf geochronology and trace element distribution in garnet: Implications for uplift and exhumation of ultra-high pressure granulites in the Sudetes, SW Poland. Lithos, 95, 363–380.

Auzanneau, E., Vielzeuf, D., and Schmidt, M.W. (2006) Experimental evidence of decompression melting during exhumation of subducted continental crust. Contributions to Mineralogy and Petrology, 152, 125–148.

Auzanneau, E., Schmidt, M.W., Vielzeuf, D., and Connolly, J.A.D. (2010) Titanium in phengite: a geobarometer for high temperature eclogites. Contributions to Mineralogy and Petrology, 159, 1–24.

Bebout, G., Ryan, J., Leeman, W., and Bebout, A. (1999) Fractionation of trace elements by subduction-zone metamorphism - effect of convergent-margin thermal evolution. Earth And Planetary Science LetterS, 171, 63–81.

Buslov, M.M., Ryabinin, A.B., Zhimulev, F.I., and Travin, A.V. (2009) Manifestations of the Late Carboniferous and Early Permian stages of formation of nappe-fold structures in the southern framework of the Siberian platform (East Sayany, South Siberia). Doklady Earth Sciences, 428, 1105–1108.

Buslov, M.M., Zhimulev, F.I., and Travin, A.V. (2010) New data on the structural setting and Ar-40/Ar-39 age of the MP-LP metamorphism of the Daulet formation, Kokchetav metamorphic belt, Northern Kazakhstan, and their tectonic interpretation. DOKLADY EARTH SCIENCES, 434, 1147–1151.

Caddick, M.J., Konopásek, J., and Thompson, A.B. (2010) Preservation of Garnet Growth Zoning and the Duration of Prograde Metamorphism. Journal of Petrology, 51, 2327–2347.

Carlson, W.D. (2012) Rates and mechanism of Y, REE, and Cr diffusion in garnet. American Mineralogist, 97, 1598–1618.

Carswell, D., Cuthbert, S., and Ravna, E. (1999) Ultrahigh-pressure metamorphism in the Western Gneiss Region of the Norwegian Caledonides. International Geology Review, 41, 955–966.

Cartigny, P., De Corte, K., Shatsky, V., Ader, M., De Paepe, P., Sobolev, N., and Javoy, M. (2001) The origin and formation of metamorphic microdiamonds from the Kokchetav massif, Kazakhstan: a nitrogen and carbon isotopic study. Chemical Geology, 176, 265–281.

Cherniak, D.J., Watson, E.B., Grove, M., and Harrison, T.M. (2004) Pb diffusion in monazite: a combined RBS/SIMS study1. Geochimica et Cosmochimica Acta, 68, 829–840.

Chopin, C. (2003) Ultrahigh-pressure metamorphism: tracing continental crust into the mantle. Earth and Planetary Science Letters, 212, 1–14.

Claoue-Long, J., Sobolev, N., Shatsky, V., and Sobolev, A. (1991) Zircon response to diamond-pressure metamorphism in the Kokchetav massif, USSR. Geology, 19, 710–713.

Dobretsov, N., and Shatsky, V. (2004) Exhumation of high-pressure rocks of the Kokchetav massif: facts and models. Lithos, 78, 307–318.

Dobretsov, N., Buslov, M., Zhimulev, F., Travin, A., and Zayachkovsky, A. (2006) Vendian-Early Ordovician geodynamic evolution and model for exhumation of ultrahighand high-pressure rocks from the Kokchetav subduction-collision zone (northern Kazakhstan). Russian Geology and Geophysics, 47, 424–440.

Dobretsov, N.L., and Buslov, M.M. (2007) Late Cambrian-Ordovician tectonics and geodynamics of Central Asia. Russian Geology and Geophysics, 48, 71–82.

Dobretsov, N.L., Sobolev, N.V., Shatsky, V.S., Coleman, R.G., and Ernst, W.G. (1995) Geotectonic evolution of diamondiferous paragneisses of the Kokchetav Complex, Northern Kazakhstan - the geologic enigma of ultrahigh-pressure crustal rocks within Phanerozoic foldbelt. The Island Arc, 4, 267–279.

Dobrzhinetskaya, L., Braun, T., Sheshkel, G., and Podkuiko, Y. (1994) Geology and structure of diamond-bearing rocks of the Kokchetav massif (Kazakhstan). Tectonophysics, 233, 293–313.

Eggins, S.M., Rudnick, R.L., and McDonough, W.F. (1998) The composition of peridotites and their minerals: a laser-ablation ICP-MS study. Earth and Planetary Science Letters, 154, 53–71.

Engvik, A., Austrheim, H., and Erambert, M. (2001) Interaction between fluid flow, fracturing and mineral growth during eclogitization, an example from the Sunnfjord area, Western Gneiss Region, Norway. Lithos, 57, 111–141.

Ewing, T.A., Hermann, J., and Rubatto, D. (2013) The robustness of the Zr-in-rutile and Ti-in-zircon thermometers during high-temperature metamorphism (Ivrea-Verbano Zone, northern Italy). Contributions to Mineralogy and Petrology, 165, 757–779.

Ferriss, E.D.A., Essene, E.J., and Becker, U. (2008) Computational study of the effect of pressure on the Ti-in-zircon geothermometer. European Journal of Mineralogy, 20, 745–755.

Ferry, J.M., and Watson, E.B. (2007) New thermodynamic models and revised calibrations for the Ti-in-zircon and Zr-in-rutile thermometers. Contributions to Mineralogy and Petrology, 154, 429–437.

Forster, M.A., Lister, G.S., Compagnoni, R., Giles, D., Hills, Q., Betts, P., Beltrando, M., Tamagno, E., G, I.P., and Venturini C. (Eds), . (2004) Mapping of oceanic crust with “HP” to “UHP” metamorphism: The Lago di Cignana Unit, (Western Alps). In G. Pasquaré and C. Venturini, Eds., Mapping Geology in Italy pp. 279–288. SELCA, Firenze.

Gerya, T. (2011) Future directions in subduction modeling. Journal Of Geodynamics, 52, 344–378.

Glorie, S., Zhimulev, F.I., Buslov, M.M., Andersen, T., Plavsa, D., Izmer, A., Vanhaecke, F., and De Grave, J. (2015) Formation of the Kokchetav subduction–collision zone (northern Kazakhstan): Insights from zircon U–Pb and Lu–Hf isotope systematics. Gondwana Research.

Hermann, J. (2002) Experimental constraints on phase relations in subducted continental crust. Contributions To Mineralogy And Petrology, 143, 219 – 235.

Hermann, J., and Rubatto, D. (2003) Relating zircon and monazite domains to garnet growth zones: age and duration of granulite facies metamorphism in the Val Malenco lower crust. Journal Of Metamorphic Geology, 21, 833 – 852.

——— (2012) Subduction of continental crust to mantle depth: Geochemistry of ultrahigh-\-pressure rocks. In Treatise on Geochemistry. Elsevier.

——— (2014) Subduction of Continental Crust to Mantle Depth: Geochemistry of Ultrahigh-Pressure Rocks. In H.D. Holland and K.K. Turekian, Eds., Treatise on Geochemistry (Second Edition) pp. 309–340. Elsevier, Oxford.

Hermann, J., and Spandler, C.J. (2008) Sediment melts at sub-arc depths: An experimental study. Journal Of Petrology, 49, 717 – 740.

Hermann, J., Rubatto, D., Korsakov, A., and Shatsky, V.S. (2001) Multiple zircon growth during fast exhumation of diamondiferous, deeply subducted continental crust (Kokchetav Massif, Kazakhstan). Contributions To Mineralogy And Petrology, 141, 66 – 82.

Holloway, J.R., and Wood, B.J. (1988) Simulating the Earth - Experimental geochemistry. Springer.

John, T., and Schenk, V. (2003) Partial eclogitisation of gabbroic rocks in a late Precambrian subduction zone (Zambia): prograde metamorphism triggered by fluid infiltration. Contributions to Mineralogy and Petrology, 146, 174–191.

Kaneko, Y., Maruyama, S., Terabayashi, M., Yamamoto, H., Ishikawa, M., Anma, R., Parkinson, C.D., Ota, T., Nakajima, Y., Katayama, I., and others (2000) Geology of the Kokchetav UHP-HP metamorphic belt, Northern Kazakhstan. Island Arc, 9, 264 – 283.

Katayama, I., Zayachkovsky, A.A., and Maruyama, S. (2000) Prograde pressure-temperature records from inclusions in zircons from ultrahigh-pressure-high-pressure rocks of the Kokchetav Massif, northern Kazakhstan. Island Arc, 9, 417 – 427.

Katayama, I., Maruyama, S., Parkinson, C., Terada, K., and Sano, Y. (2001) Ion micro-probe U-Pb zircon geochronology of peak and retrograde stages of ultrahigh-pressure metamorphic rocks from the Kokchetav massif, northern Kazakhstan. Earth and Planetary Science Letters, 188, 185–198.

Konrad-Schmolke, M., Zack, T., O'Brien, P.J., and Jacob, D.E. (2008) Combined thermodynamic and rare earth element modelling of garnet growth during subduction: Examples from ultrahigh-pressure eclogite of the Western Gneiss Region, Norway. Earth and Planetary Science Letters, 272, 488–498.

Korsakov, A., Shatskii, V., and Sobolev, N. (1998) First occurrence of coesite in eclogites from Kokchetav massif. Doklady Akademii Nauk, 360, 77–81.

Korsakov, A.V., Shatsky, V.S., Sobolev, N.V., and Zayachokovsky, A.A. (2002) Garnet-biotite-clinozoisite gneiss: a new type of diamondiferous metamorphic rock from the Kokchetav Massif. European Journal of Mineralogy, 14, 915 – 928.

Korsakov, A.V., Theunissen, K., Kozmenko, O.A., and Ovchinnikov, Y.I. (2006) Reaction textures in clinozoisite gneisses. Russian Geology and Geophysics, 47, 497 – 510.

Korsakov, A.V., Perraki, M., Zhukov, V.P., De Gussem, K., Vandenabeele, P., and Tomilenko, A.A. (2009) Is quartz a potential indicator of ultrahigh-pressure metamorphism? Laser Raman spectroscopy of quartz inclusions in ultrahigh-pressure garnets. European Journal of Mineralogy, 21, 1313–1323.

Kotková, J., and Harley, S.L. (2010) Anatexis during High-pressure Crustal Metamorphism: Evidence from Garnet–Whole-rock REE Relationships and Zircon–Rutile Ti–Zr Thermometry in Leucogranulites from the Bohemian Massif. Journal of Petrology, 51, 1967–2001.

Lavrova, L.D., Pechnikov, V.A., Petrova, M.A., and Zayachkovsky, A.A. (1996) Geology of the Barchi diamondiferous area. Otechestvennaya Geologiya, 12, 12–27.

Lee†, J.K.W., Williams, I.S., and Ellis, D.J. (1997) Pb, U and Th diffusion in natural zircon. Nature, 390, 159–162.

Letnikov, F., Kostitsyn, Y., Vladykin, N., Zayachkovskii, A., and Mishina, E. (2004) Isotopic characteristics of the Krasnyi Mai ultramafic alkaline rock complex, northern Kazakhstan. Doklady Earth Sciences, 399A, 1315–1319.

Liou, J.G., Zhang, R.Y., Katayama, I., Maruyama, S., and Ernst, W.. (2002) Petrotectonic characterization f the Kokchetav Massif and the Dabie-Sulu terranes Ultrahigh-P metamorphism in the so-called P-T Forbidden-Zone. Western Pacific Earth Sciences, 2, 119–148.

Liu, F., Xua, Z., Katayama, I., Yang, J., Maruyama, S., and Liou, J. (2001) Mineral inclusions in zircons of para- and orthogneiss from pre-pilot drillhole CCSD-PP1, Chinese Continental Scientific Drilling Project. Lithos, 59, 199–215.

Liu, F., Xu, Z., Liou, J., Katayama, I., Masago, H., Maruyama, S., and Yang, J. (2002) Ultrahigh-pressure mineral inclusions in zircons from gneissic core samples of the Chinese Continental Scientific Drilling Site in eastern China. European Journal of Mineralogy, 14, 499–512.

 44

Liu, F., Xu, Z., Liou, J.G., Dong, H., and Xue, H. (2007) Ultrahigh-pressure mineral assemblages in zircons from surface to 5158 m depth cores in the main drill hole of Chinese Continental Scientific Drilling Project, southwestern Sulu belt, China. International Geological Review, 49, 454–478.

Ludwig, K. (2003) User's manual for Isoplot 3.00. A geochronological Toolkit for Microsoft Excel. Berkeley Geochronology Center, Berkeley, California.

Masago, H. (2000) Metamorphic petrology of the Barchi-Kol metabasites, western Kokchetav ultrahigh-pressure-high-pressure massif, northern Kazakhstan. Island Arc, 9, 358–378.

Massonne, H. (2003) A comparison of the evolution of diamondiferous quartz-rich rocks from the Saxonian Erzgebirge and the Kokchetav Massif: are so-called diamondiferous gneisses magmatic rocks? Earth and Planetary Science Letters, 216, 347–364.

Massonne, H.-J., Willner, A.P., and Gerya, T. (2007) Densities of metapelitic rocks at high to ultrahigh pressure conditions: What are the geodynamic consequences? Earth and Planetary Science Letters, 256, 12–27.

McDonough, W., and Sun, S. (1995) The composition of the earth. Chemical Geology, 120, 223–253.

Nadolinny, V.A., Shatsky, V.S., Kozmenko, O.A., Stepanov, A.S., Palyanov, Y.N., and Kupriyanov, I.N. (2006) Study of local concentration of single substitutional nitrogen atoms in microdiamonds from the Kokchetav massif. European Journal of Mineralogy, 18, 739–743.

Norman, M., Griffin, W., Pearson, N., Garcia, M., and O'Reilly, S. (1998) Quantitative analysis of trace element abundances in glasses and minerals: a comparison of laser ablation inductively coupled plasma mass spectrometry, solution inductively coupled plasma mass spectrometry, proton microprobe and electron microprobe data. Journal Of Analytical Atomic Spectrometry, 13, 477–482.

Ogasawara, Y., Fukasawa, K., and Maruyama, S. (2002) Coesite exsolution from supersilicic titanite in UHP marble from the Kokchetav Massif, northern Kazakhstan. American Mineralogist, 87, 454–461.

Parkinson, C. (2000) Coesite inclusions and prograde compositional zonation of garnet in whiteschist of the HP-UHPM Kokchetav massif, Kazakhstan: a record of progressive UHP metamorphism. Lithos, 52, 215–233.

Pearce, N.J.G., Perkins, W.T., Westgate, J.A., Gorton, M.P., Jackson, S.E., Neal, C.R., and Chenery, S.P. (1997) A Compilation of New and Published Major and Trace Element Data for NIST SRM 610 and NIST SRM 612 Glass Reference Materials. Geostandards Newsletter, 21, 115–144.

Peterman, E.M., Hacker, B.R., and Baxter, E.F. (2009) Phase transformations of continental crust during subduction and exhumation: Western Gneiss Region, Norway. European Journal of Mineralogy, 21, 1097–1118.

Plank, T., and Langmuir, C. (1998) The chemical composition of subducting sediment and its consequences for the crust and mantle. Chemical Geology, 145, 325–394.

Pyle, J., Spear, F.S., Rudnick, R., and Mcdonough, W.F. (2001) Monazite-Xenotime-Garnet Equilibrium in Metapelites and a New Monazite-Garnet Thermometer. J. Petrology, 42, 2083–2107.

Ragozin, A.L., Liou, J.G., Shatsky, V.S., and Sobolev, N.V. (2009) The timing of the retrograde partial melting in the Kumdy-Kol region (Kokchetav Massif, Northern Kazakhstan). Lithos, 109, 274–284.

 45

Ravna, E., and Terry, M. (2004) Geothermobarometry of UHP and HP eclogites and schists - an evaluation of equilibria among garnet-clinopyroxene-kyanite-phengite-coesite/quartz. Journal of Metamorphic Geology, 22, 579–592.

Rozen, O. (1971) Rifean in the Kokchetav massif. Proceedings of USSR Academy of science, 7, 102–104.

Rubatto, D. (2002) The link between U-Pb ages of accessory minerals and metamorphic conditions. Geochimica Et Cosmochimica Acta, 66, A653 – A653.

Rubatto, D., Williams, I.S., and Buick, I.S. (2001) Zircon and monazite response to prograde metamorphism in the Reynolds Range, central Australia. Contributions to Mineralogy and Petrology, 140, 458–468.

Rubatto, D., Hermann, J., and Buick, I.S. (2006) Temperature and bulk composition control on the growth of monazite and zircon during low-pressure anatexis (Mount Stafford, central Australia). Journal Of Petrology, 47, 1973 – 1996.

Schertl, H.-P., and Sobolev, N.V. (2013) The Kokchetav Massif, Kazakhstan: “Type locality” of diamond-bearing UHP metamorphic rocks. Journal of Asian Earth Sciences, 63, 5–38.

Shatsky, V.S., Jagoutz, E., Sobolev, N.V., Koz’menko, O.A., Parkhomenko, V.S., and Troesch, M. (1999) Geochemistry and age of ultrahigh pressure metamorphic rocks from the Kokchetav massif (Northern Kazakhstan). Contributions to Mineralogy and Petrology, 137, 185–205.

Shatsky, V.S., Sobolev, N.V., Korsakov, A.V., Ragozin, A.L., and Zayachkovsky, A.A. (2005) A new occurrence of diamondiferous rocks in Kokchetav massif (Northern Kazakhstan). In Proceedings of Eclogite conference 2005.

Sitnikova, E.S., and Shatsky, V.S. (2009) New FTIR spectroscopy data on the composition of the medium of diamond crystallization in metamorphic rocks of the Kokchetav Massif. Russian Geology and Geophysics, 50, 842–849.

Sobolev, N., and Shatsky, V. (1990) Diamond inclusions in garnets from metamorphic rocks - a new environment for diamond formation. Nature, 343, 742–746.

Sobolev, N., Shatskii, V., Vavilov, M., and Goryainov, S. (1991) Coesite inclusion in zircon from diamond-containing gneisses of Kokchetav massif - 1st find of coesite in metamorphic rocks in the USSR. Doklady Akademii Nauk SSSR, 321, 184–188.

——— (1994) Zircon from high-pressure metamorphic rocks of folded regions as an unique container of inclusions of diamond, coesite and coexisting minerals. Doklady Akademii Nauk, 334, 488–492.

Sobolev, N.V., Schertl, H.-P., Valley, J.W., Page, F.Z., Kita, N.T., Spicuzza, M.J., Neuser, R.D., and Logvinova, A.M. (2011) Oxygen isotope variations of garnets and clinopyroxenes in a layered diamondiferous calcsilicate rock from Kokchetav Massif, Kazakhstan: a window into the geochemical nature of deeply subducted UHPM rocks. Contributions to Mineralogy and Petrology, 162, 1079–1092.

Spear, F.S., and Pyle, J.M. (2010) Theoretical modeling of monazite growth in a low-Ca metapelite. Chemical Geology, 273, 111–119.

Stepanov, A.S., Hermann, J., Rubatto, D., and Rapp, R.P. (2012) Experimental study of monazite/melt partitioning with implications for the REE, Th and U geochemistry of crustal rocks. Chemical Geology, 300-301, 200–220.

 46

Stepanov, A.S., Hermann, J., Korsakov, A.V., and Rubatto, D. (2014) Geochemistry of ultrahigh-pressure anatexis: fractionation of elements in the Kokchetav gneisses during melting at diamond-facies conditions. Contributions to Mineralogy and Petrology, 167, 1–25.

Storre, B. (1972) Dry melting of muscovite+quartz in the range P s=7 kb to P s=20 kb. Contributions to Mineralogy and Petrology, 37, 87–89.

Syracuse, E.M., van Keken, P.E., and Abers, G.A. (2010) The global range of subduction zone thermal models. Physics of the Earth and Planetary Interiors, 183, 73–90.

Tailby, N.D., Walker, A.M., Berry, A.J., Hermann, J., Evans, K.A., Mavrogenes, J.A., O'Neill, H.S.C., Rodina, I.S., Soldatov, A.V., Rubatto, D., and others (2011) Ti site occupancy in zircon. Geochimica et Cosmochimica Acta, 75, 905–921.

Tirone, M., Ganguly, J., Dohmen, R., Langenhorst, F., Hervig, R., and Becker, H.-W. (2005) Rare earth diffusion kinetics in garnet: Experimental studies and applications. Geochimica et Cosmochimica Acta, 69, 2385–2398.

Tomkins, H.S., Powell, R., and Ellis, D.J. (2007) The pressure dependence of the zirconium-in-rutile thermometer. Journal of Metamorphic Geology, 25, 703–713.

Turkina, O.M., Letnikov, F.A., and Levin, A.V. (2011) Mesoproterozoic Granitoids of the Kokchetav Microcontinent Basement. Doklady Earth Sciences, 436, 176–180.

van Keken, P., Kiefer, B., and Peacock, S. (2002) High-resolution models of subduction zones: Implications for mineral dehydration reactions and the transport of water into the deep mantle. Geochemistry Geophysics Geosystems, 3.

Van Orman, J., Grove, T., Shimizu, N., and Layne, G. (2002) Rare earth element diffusion in a natural pyrope single crystal at 2.8 GPa. Contributions to Mineralogy and Petrology, 142, 416–424.

Vavilov, M.A., Sobolev, N.V., and Shatskiy, V.S. (1993) Micas in diamond-bearing metamorphic rocks of Northern Kazakhstan. Doklady. Earth science sections, 319 A, 177–182.

Wang, C.Y., Campbell, I.H., Stepanov, A.S., Allen, C.M., and Burtsev, I.N. (2011) Growth rate of the preserved continental crust: II. Constraints from Hf and O isotopes in detrital zircons from Greater Russian Rivers. Geochimica et Cosmochimica Acta, 75, 1308–1345.

Warren, C.J., Beaumont, C., and Jamieson, R.A. (2008) Modelling tectonic styles and ultra-high pressure (UHP) rock exhumation during the transition from oceanic subduction to continental collision. Earth and Planetary Science Letters, 267, 129–145.

Williams, I. (1998) U-Th-Pb geochronology by ion microprobe. In W.S. M. McKibben and W. Ridley, Eds., Applications of Microanalytical Techniques to Understanding Mineralizing Process Vol. 7, pp. 1–36. Society of Economic Geologists, Inc.

Yang, P., and Pattison, D. (2006) Genesis of monazite and Y zoning in garnet from the Black Hills, South Dakota. Lithos, 88, 233–253.

Zhang, R., Liou, J., Ernst, W., Coleman, R., Sobolev, N., and Shatsky, V. (1997) Metamorphic evolution of diamond-bearing and associated rocks from the Kokchetav Massif, northern Kazakhstan. Journal of Metamorphic Geology, 15, 479–496.

47

Zheng, Y.-F., Gao, X.-Y., Chen, R.-X., and Gao, T. (2011) Zr-in-rutile thermometry of eclogite in the dabie orogen: constraints on rutile growth during continental subduction-zone metamorphism. Journal of Asian Earth Sciences, 40, 427–451.

Zhimulev, F.I. (2007) The Tectonics and Early Ordovician Geodynamic Evolution of the Kokchetav HP-UHP Metamorphic Belt. IGM SO RAN, Novosibirsk.

Zhimulev, F.I., Poltaranina, M.A., Korsakov, A.V., Buslov, M.M., Druzyaka, N.V., and Travin, A.V. (2010) Eclogites of the Late Cambrian-Early Ordovician North Kokchetav tectonic zone (northern Kazakhstan): structural position and petrology. Russian Geology and Geophysics, 51, 190–203.

Zhimulev, F.I., Buslov, M.M., Travin, A.V., Dmitrieva, N.V., and De Grave, J. (2011) Early-Middle Ordovician nappe tectonics of the junction between the Kokchetav HP-UHP metamorphic belt and the Stepnyak paleoisland arc (northern Kazakhstan). Russian Geology and Geophysics, 52, 109–123.

Zonenshain, L., Kuzmin, M., and Natapov, L. (1990) Geology of the USSR: a plate-tectonic synthesis, 242 p. AGU.

 48

Figure 1. a) Simplified map of the Kokchetav complex based on the map by Zhimulev (2007). b) Map of Barchi-Kol area and sample locations (red labels) compiled from maps by Korsakov et al. (2002) and Masago (2000). High-pressure, medium temperature units (High-P, medium-T) units are given according to Masago (2000). The samples with different PT paths are situated within the UHP terrain. For the colored version of this and following figures, the reader is referred to the electronic version of the paper.

Figure 2. Petrographic features of the studied samples on photographs, transmitted light and SEM images. a – b Sample B01-3. a) Thin section of the sample B01-3 with large and small garnet grains and large phengite flakes. b) Garnet porphyroblast with LA-ICP-MS profile and enlargement of the core zone with inclusions of quartz and xenotime. (c – e) Sample B94-333 c, d) scans of the sample show the gneissic texture with large garnet grains in one part of the sample. e) Large garnet with inclusions of rutile, monazite and quartz in the mantle surrounded by the matrix of quartz, feldspars and biotite. (f – g) Scan of sample and thin section of sample B94-256, showing a foliation and association of biotite with phengite and garnet. h) Inclusions of rutile and mica aggregates in garnet showing replacement of phengite by biotite. (i–k) Sample B118A50. i) Scan of sample and of thin section (j) showing gneissic texture of the rock with millimeter scale layers enriched in quartz and feldspar. k) Photo of the thin section with inset showing zircon with a diamond inclusion. Note the difference in texture between samples B94-333 and B118A50, which have gneissic texture, and samples B01-3 and B94-256, which display a strong foliation.

Figure 3. Electron microprobe element maps of garnet (a–d, g–h) and phengite zoning (e–f) from samples B01-3 (a–f) and B94-256 (g–h).

Figure 4. Garnet REE patterns normalized to chondrite (McDonough and Sun 1995)(McDonough and Sun 1995).

Figure 5. Composition of garnet and phengite found in the matrix and as inclusions in other minerals. Mnz inc – inclusions in monazite, Zrn inc – inclusions in zircon, Grt inc – inclusions in garnet. Gray arrows demonstrate proposed evolution of phengite composition.

Figure 6. Major element profiles across garnet grains from the four investigated samples.

Figure 7. Profiles of selected trace elements across garnet grains from the four investigated samples.

Figure 8. Back scattered electron images of monazite crystals. Circles mark location of LA-ICP-MS and SHRIMP analyses and numbers show U-Pb dates in Ma±1σ and Y contents.

Figure 9. Trace element composition of monazite from studied samples and also allanite from micaschist B94-256 normalized to chondrite (McDonough and Sun 1995).

Figure 10: Results of SHRIMP U-Pb dating of monazite and zircon. Data-point error ellipses are 2σ.

Figure 11. REE patterns of zircons normalized to chondrite (McDonough and Sun 1995).

Figure 12. Zircon internal zoning revealed by CL imaging. Circles show spots of LA-ICP-MS and SHRIMP analyses (Ma±1σ) and numbers show U-Pb dates in Ma ±1σ.

Figure 13. Temperatures calculated by from solubility of Ti in zircon using the Ferry and Watson (2007) calibration.

 50

Figure 14. a) Estimates of PT paths for the rocks of the Kokchetav complex from various studies. 1–Dobretsov and Shatsky (2004), 2–Zhang et al. (1997), 3–Hermann et al. (2001), 4–Auzanneau et al. (2006), 5–Massonne (2003), 6–Katayama et al. (2001). b) Proposed PT paths for studied samples. Ellipses represent uncertainty on PT estimates. The PT path of B118A50 is based on Hermann et al (2001) with changes according to(Auzanneau et al. 2006). Gray lines show location of reactions of phengite breakdown, with phengite disappearance right/below lines: (a) reaction Ms(Phe)+Qtz(Coe)=K-Fsp +Al_2SiO_5+melt from Storre (1972) and Auzanneau et al. (2006), (b) reaction Cpx+Phe+Qtz=Bt+Pl+Grt+melt (Auzanneau et al. 2006), (c) phengite upper stability limit (Hermann and Spandler, 2008).

Figure 15. Summary of U-Pb SHRIMP ages obtained in this study and comparison with results of previous investigations (Claoue-Long et al. 1991; Hermann et al. 2001; Katayama et al. 2001; Ragozin et al. 2009). Colored rectangles show relative proportion of zircon/monazite growth during prograde/peak/retrogression of the rock. Gray diamonds represent averages, with error bars for 95 % confidence interval or as reported in original studies; black diamonds show highest and lowest values obtained in individual measurements. D1–D4 ages of different zircon domains from study by Hermann et al (2001).

Table 1. Comparison of various petrological parameters of studied samples.

		B01-3	**B94-333**	**B94-256**	**B118A50**
Rock type		Ky-micaschist	Layered gneiss	Micaschist	Diamond-bearing gneiss
Major minerals		Grt, Ky, Q, Phe	Grt, Pl, Ky, Phe, Bt	Grt, Q, Kfsp, Phe, Bt	Grt, Q, Kfsp, Pl, Bt, Phe, Rt
Accessory minerals		Rt, Zrn, Mnz, Ap	Rt, Zrn, Mnz, Ap	Rt, Zrn, Mnz, Aln, Ap	Rt, Zrn, Aln
Grt major zoning		prograde	pro-/retro-grade Ca, Mg up; HREE down	retrograde, Ca, Mn up	retrograde, Mn up
Grt REE zoning		HREE rich core	HREE rich core	HREE reach rim	HREE flat
Zircon inclusions		Grt, Phe, Q	Grt, Phe, Cpx, Coe	Grt, Phe, Coe	Dia, Coe, Phe, Cpx
Zircon ages, Ma		504±7-524±7	n.a.	522±6	503±7-532±6
Monazite ages, Ma		528±8	528±7	521±13	n.a.
T ºC, by Ti-in-rutile Tomkins et al. (2007)		670-710	830-860	≈905	870-890
T ºC, by Ti-in-zircon, Ferry and Watson (2007)		645-720	815-940	765-1080	850-1040
P-T matrix	ºC	710±20	740±30	700±20	800
	kbar	24±2	12±3	21±2	10
P-T peak	ºC	710±20	800-900	950-1000	950-1000
	kbar	24±2	29±2	≈45	49

(DOI will not work until issue is live.) DOI: http://dx.doi.org/10.2138/am-2016-5454

n.a. = not analysed

Deposit Items

Figure S1: Mineral evolution diagrams for the studied samples. Different thickness of lines demonstrates changes in mineral abundance. o — denotes homogenization of mineral by diffusion. M inc — monazite inclusions, Z inc — zircon inclusions, mtx — matrix.

Table S1: Major element compositions of garnet

Table S2: Major element compositions of garnet

Table S3: Major element compositions pyroxene inclusions

Table S4: Major element compositions of feldspar

Table S5: Trace element compositions of garnet

Table S6: Trace element compositions of rutile

Table S7: Trace element compositions of monazite

Table S8: Trace element compositions of zircon

Table S9: U, Th and Pb SHRIMP data for monazite

Table S10: U, Th and Pb SHRIMP data for zircon

 53

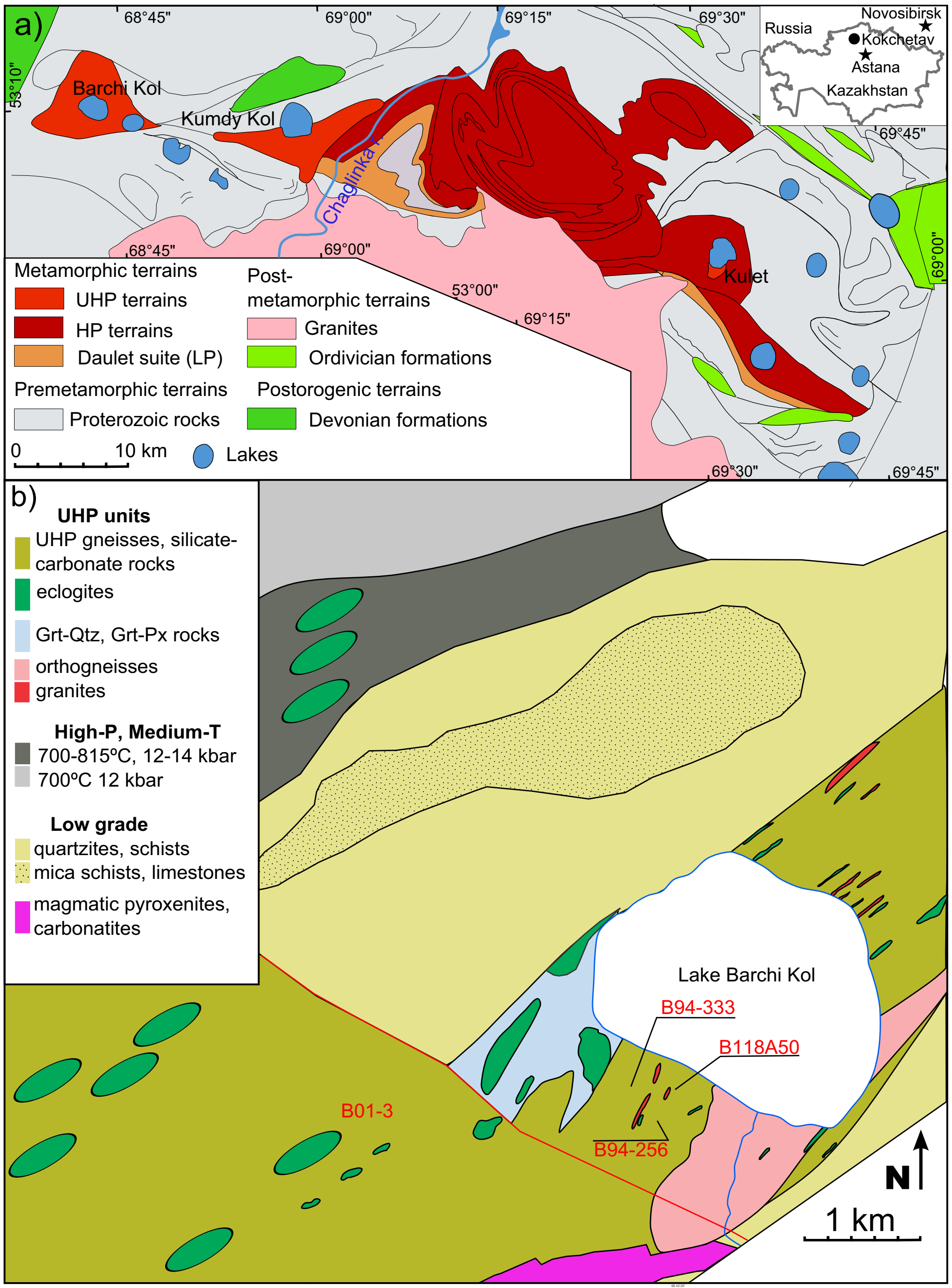
a)
68°45"
69°00"
69°15"
69°30"
53°10"
Barchi Kol
Kumdy Kol
Chaglinka r.
Kulet
Russia
Novosibirsk
Kokchetav
Astana
Kazakhstan
69°45"
69°00"
68°45"
69°00"
53°00"
69°15"
69°30"
69°45"
Metamorphic terrains
UHP terrains
HP terrains
Daulet suite (LP)
Post-metamorphic terrains
Granites
Ordivician formations
Premetamorphic terrains
Proterozoic rocks
Postorogenic terrains
Devonian formations
0
10 km
Lakes
b)
UHP units
UHP gneisses, silicate-carbonate rocks
eclogites
Grt-Qtz, Grt-Px rocks
orthogneisses
granites
High-P, Medium-T
700-815ºC, 12-14 kbar
700ºC 12 kbar
Low grade
quartzites, schists
mica schists, limestones
magmatic pyroxenites, carbonatites
Lake Barchi Kol
B94-333
B118A50
B01-3
B94-256
N
1 km

Figure 1

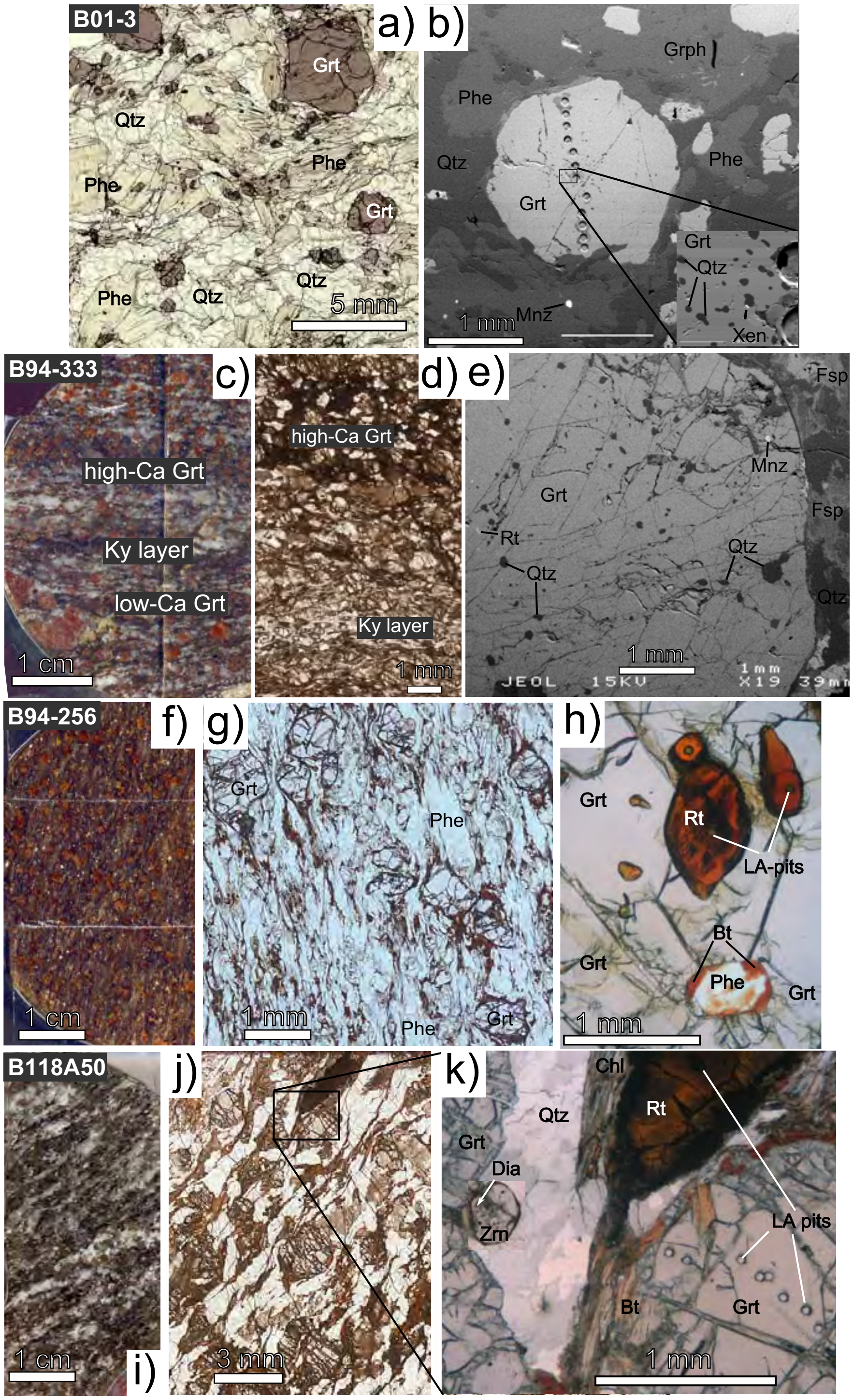
B01-3
a)
b)
Grt
Qtz
Phe
Phe
Grt
Phe
Qtz
Qtz
5 mm
Grph
Phe
Qtz
Phe
Grt
Grt
Qtz
Mnz
1 mm
Xen
B94-333
c)
d)
e)
high-Ca Grt
Ky layer
low-Ca Grt
1 cm
high-Ca Grt
Ky layer
1 mm
Fsp
Mnz
Grt
Fsp
Rt
Qtz
Qtz
Qtz
1 mm
B94-256
f)
g)
h)
1 cm
Grt
Phe
1 mm
Phe
Grt
Grt
Rt
LA-pits
Bt
Grt
Phe
Grt
1 mm
B118A50
i)
j)
k)
1 cm
3 mm
Chl
Rt
Qtz
Grt
Dia
Zrn
LA pits
Bt
Grt
1 mm

Figure 2

This is a preprint, the final version is subject to change, of the American Mineralogist (MSA)
Cite as Authors (Year) Title. American Mineralogist, in press.
(DOI will not work until issue is live.) DOI: http://dx.doi.org/10.2138/am-2016-5454

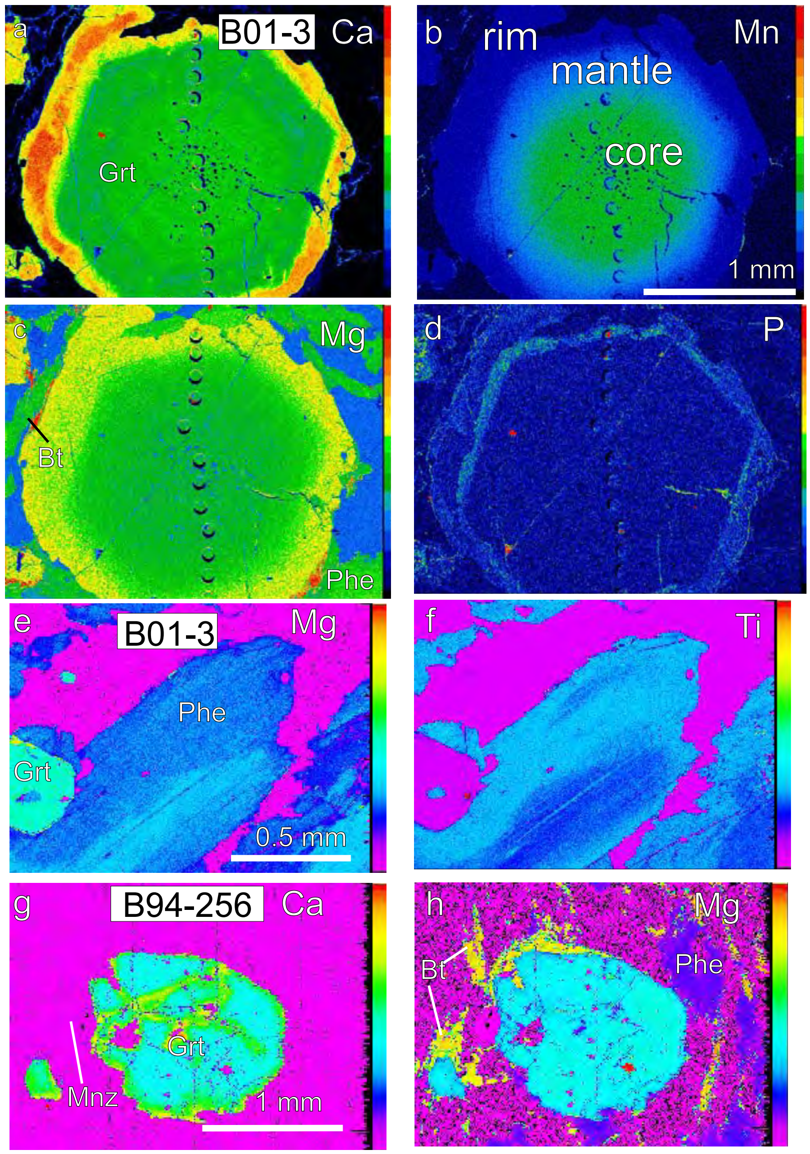

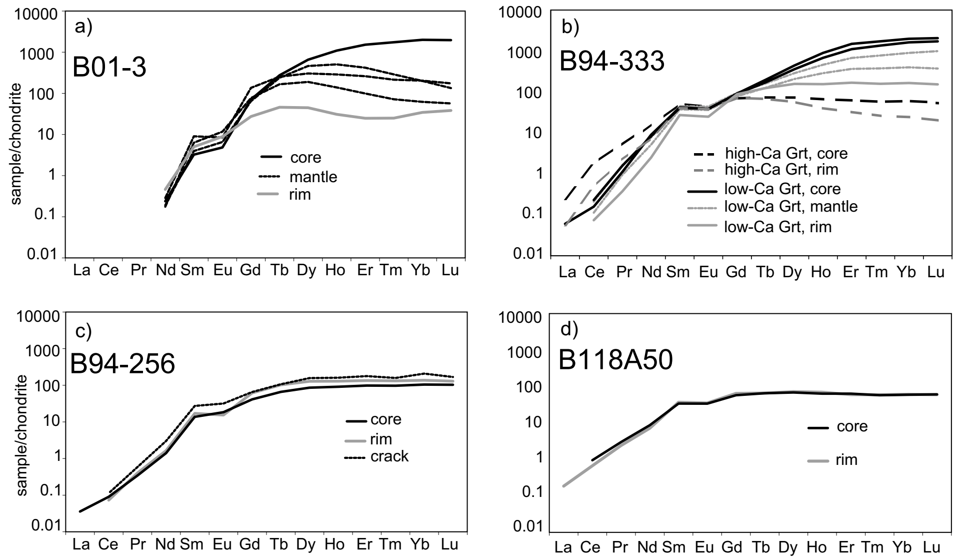
a)
B01-3
sample/chondrite
10000
1000
100
10
1
0.1
0.01
core
mantle
rim
La Ce Pr Nd Sm Eu Gd Tb Dy Ho Er Tm Yb Lu
b)
B94-333
high-Ca Grt, core
high-Ca Grt, rim
low-Ca Grt, core
low-Ca Grt, mantle
low-Ca Grt, rim
c)
B94-256
core
rim
crack
d)
B118A50
core
rim

Figure 4

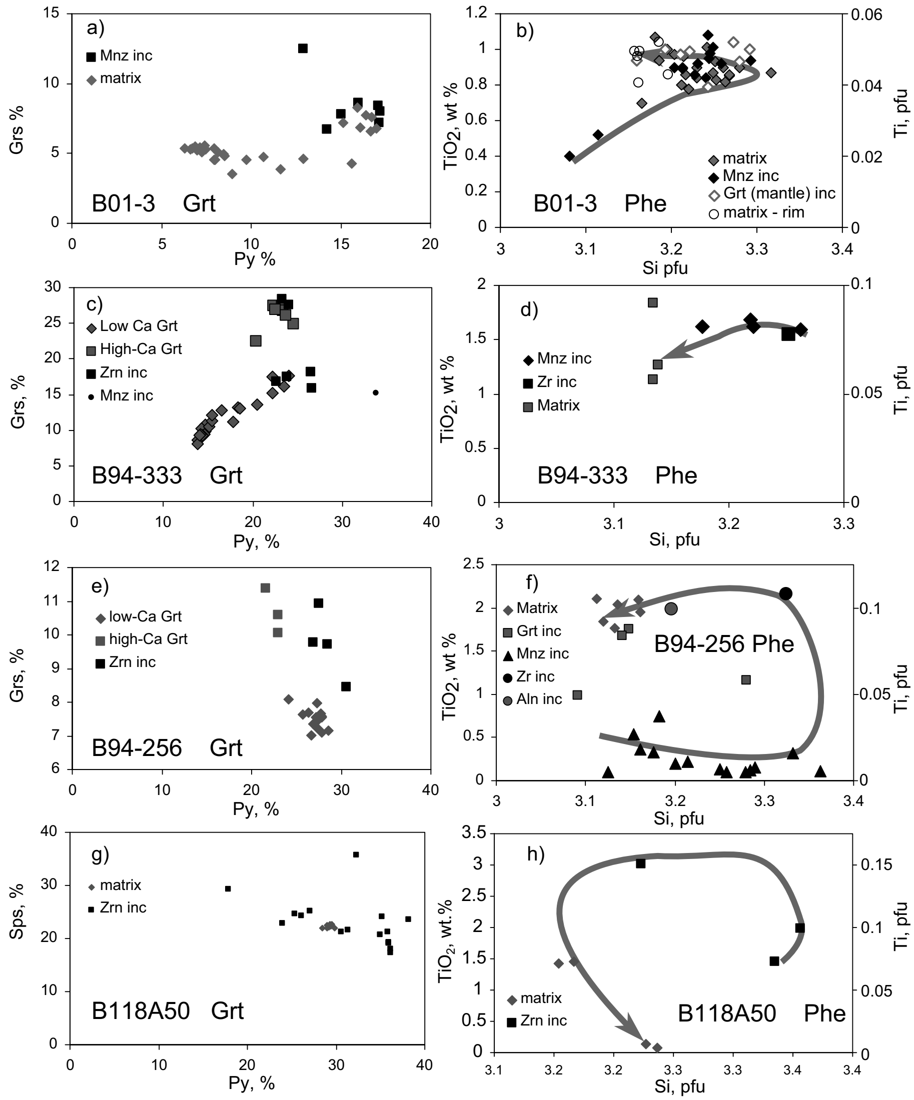
a)
Mnz inc
matrix
B01-3 Grt
Grs %
Py %
b)
B01-3 Phe
matrix
Mnz inc
Grt (mantle) inc
matrix - rim
TiO2, wt %
Ti, pfu
Si pfu
c)
Low Ca Grt
High-Ca Grt
Zrn inc
Mnz inc
B94-333 Grt
Grs, %
Py, %
d)
Mnz inc
Zr inc
Matrix
B94-333 Phe
TiO2, wt %
Ti, pfu
Si, pfu
e)
low-Ca Grt
high-Ca Grt
Zrn inc
B94-256 Grt
Grs, %
Py, %
f)
Matrix
Grt inc
Mnz inc
Zr inc
Aln inc
B94-256 Phe
TiO2, wt %
Ti, pfu
Si, pfu
g)
matrix
Zrn inc
B118A50 Grt
Sps, %
Py, %
h)
matrix
Zrn inc
B118A50 Phe
TiO2, wt.%
Ti, pfu
Si, pfu

Figure 5

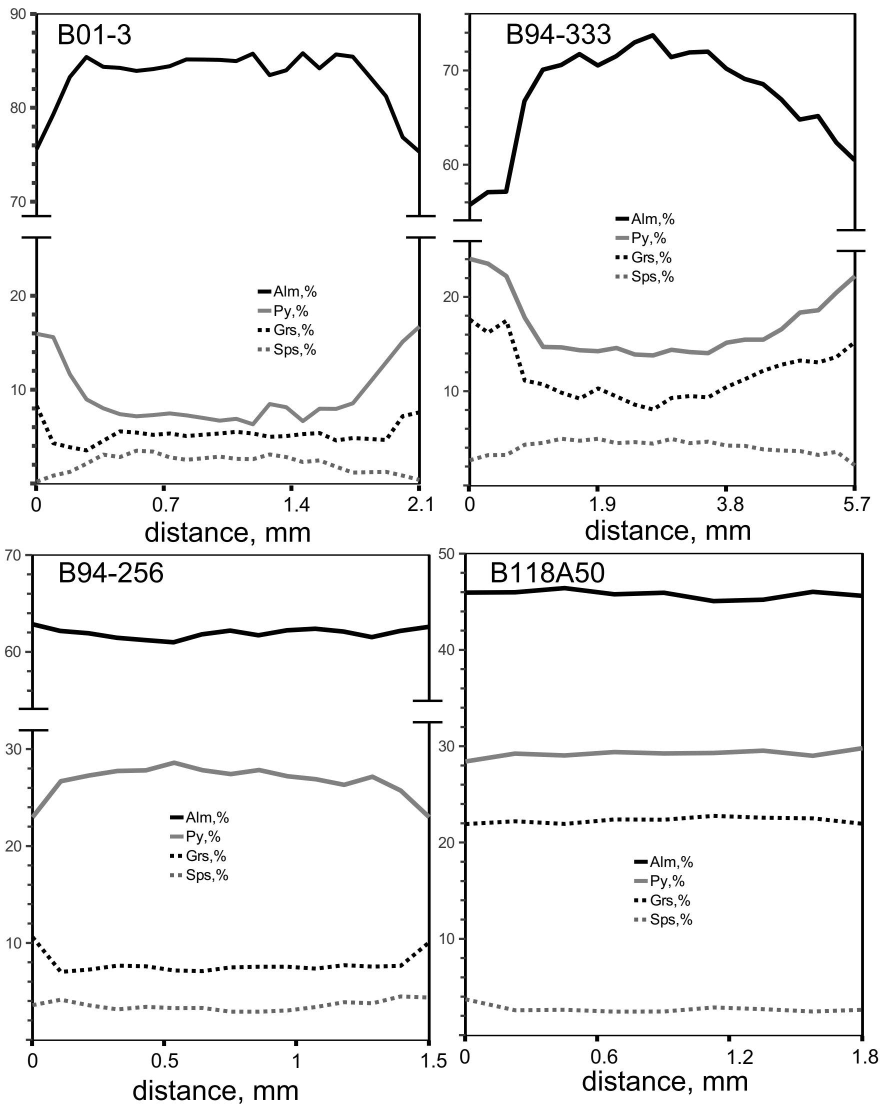
B01-3
B94-333
B94-256
B118A50
Alm,%
Py,%
Grs,%
Sps,%
distance, mm
0
0.7
1.4
2.1
1.9
3.8
5.7
0.5
1
1.5
0.6
1.2
1.8
90
80
70
60
50
40
30
20
10

Figure 6

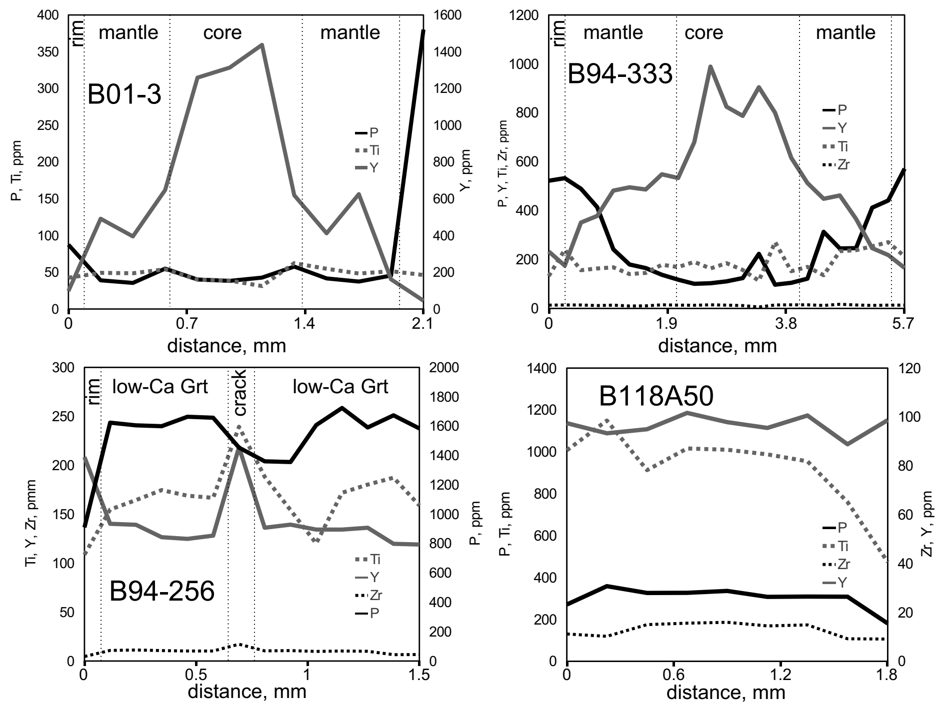
B01-3
rim
mantle
core
mantle
P
Ti
Y
P, Ti, ppm
Y, ppm
distance, mm
B94-333
rim
mantle
core
mantle
P
Y
Ti
Zr
P, Y, Ti, Zr, ppm
distance, mm
B94-256
rim
low-Ca Grt
crack
low-Ca Grt
Ti
Y
Zr
P
Ti, Y, Zr, pmm
P, ppm
distance, mm
B118A50
P
Ti
Zr
Y
P, Ti, ppm
Zr, Y, ppm
distance, mm

Figure 7

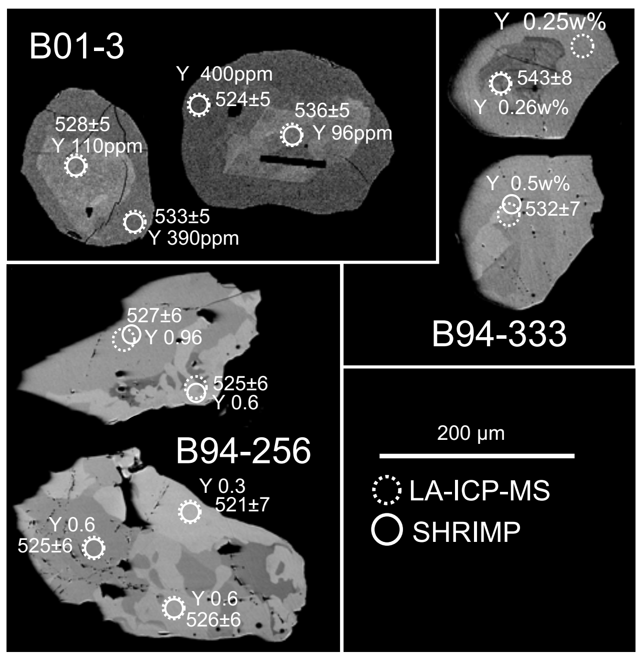
B01-3
Y 400ppm
524±5
536±5
Y 96ppm
528±5
Y 110ppm
533±5
Y 390ppm
Y 0.25w%
543±8
Y 0.26w%
Y 0.5w%
532±7
B94-333
527±6
Y 0.96
525±6
Y 0.6
B94-256
Y 0.3
521±7
Y 0.6
525±6
Y 0.6
526±6
200 μm
LA-ICP-MS
SHRIMP

Figure 8

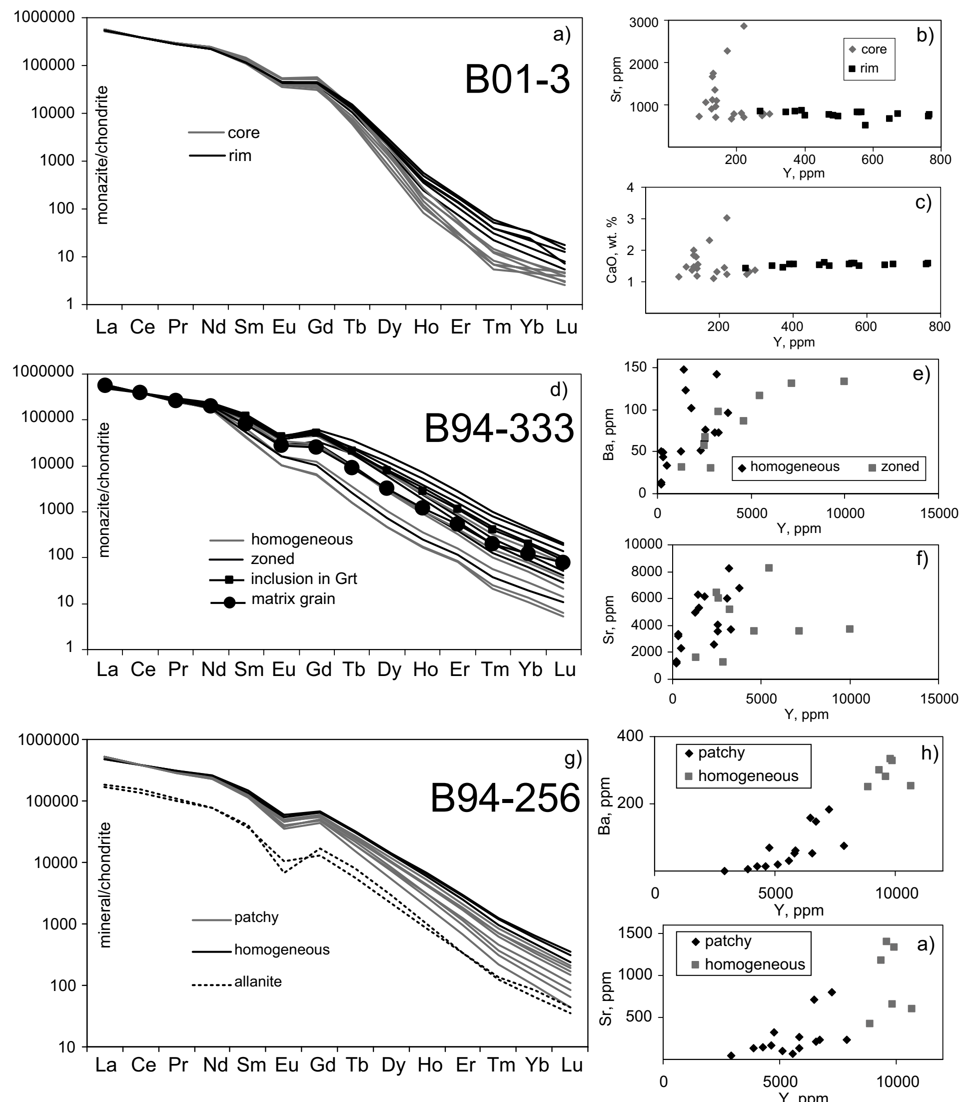
a)
B01-3
monazite/chondrite
core
rim
La Ce Pr Nd Sm Eu Gd Tb Dy Ho Er Tm Yb Lu
b)
Sr, ppm
Y, ppm
c)
CaO, wt. %
d)
B94-333
homogeneous
zoned
inclusion in Grt
matrix grain
e)
Ba, ppm
f)
g)
B94-256
mineral/chondrite
patchy
homogeneous
allanite
h)

Figure 9

This is a preprint, the final version is subject to change, of the American Mineralogist (MSA)
Cite as Authors (Year) Title. American Mineralogist, in press.
(DOI will not work until issue is live.) DOI: http://dx.doi.org/10.2138/am-2016-5454

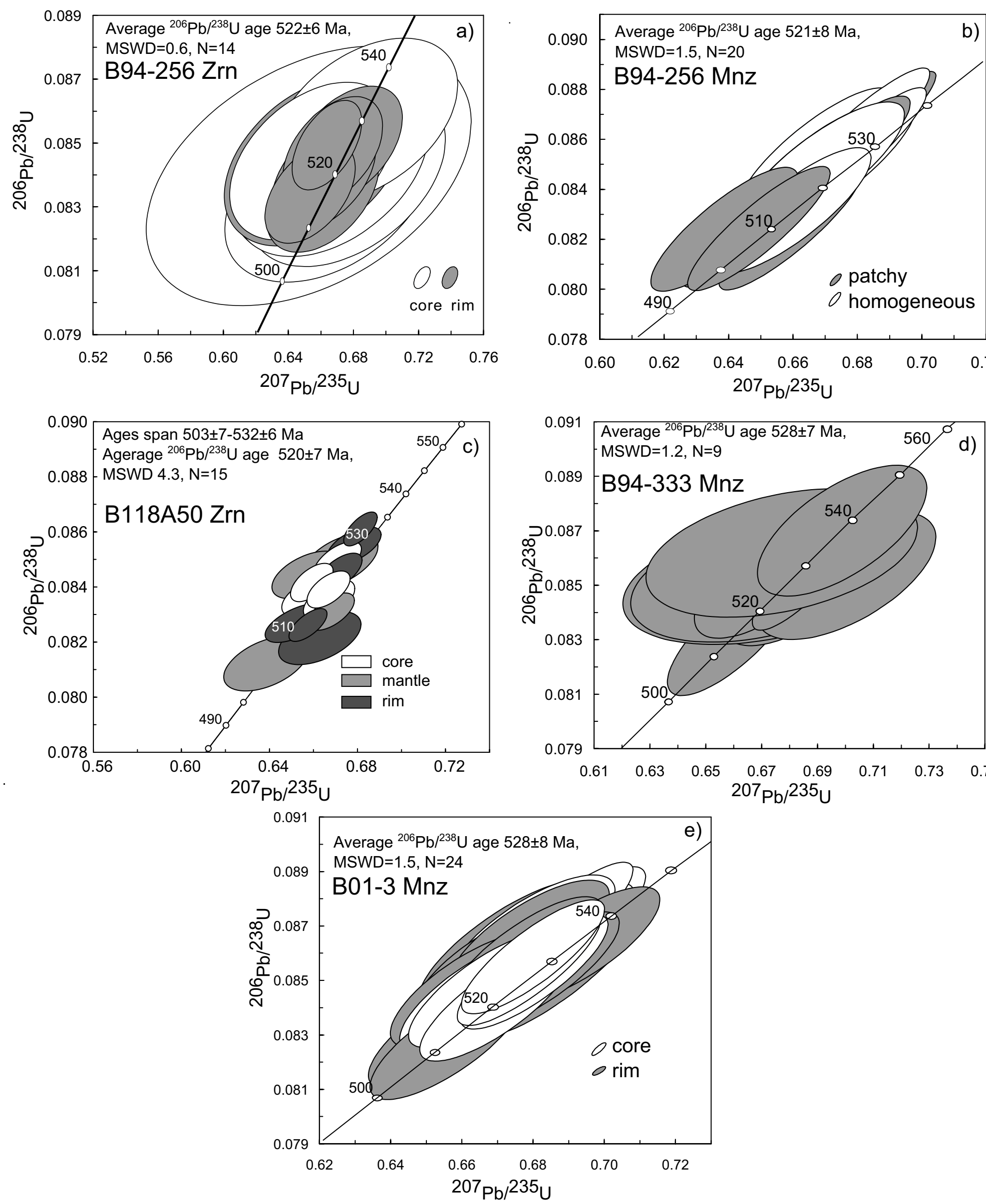

Figure 10

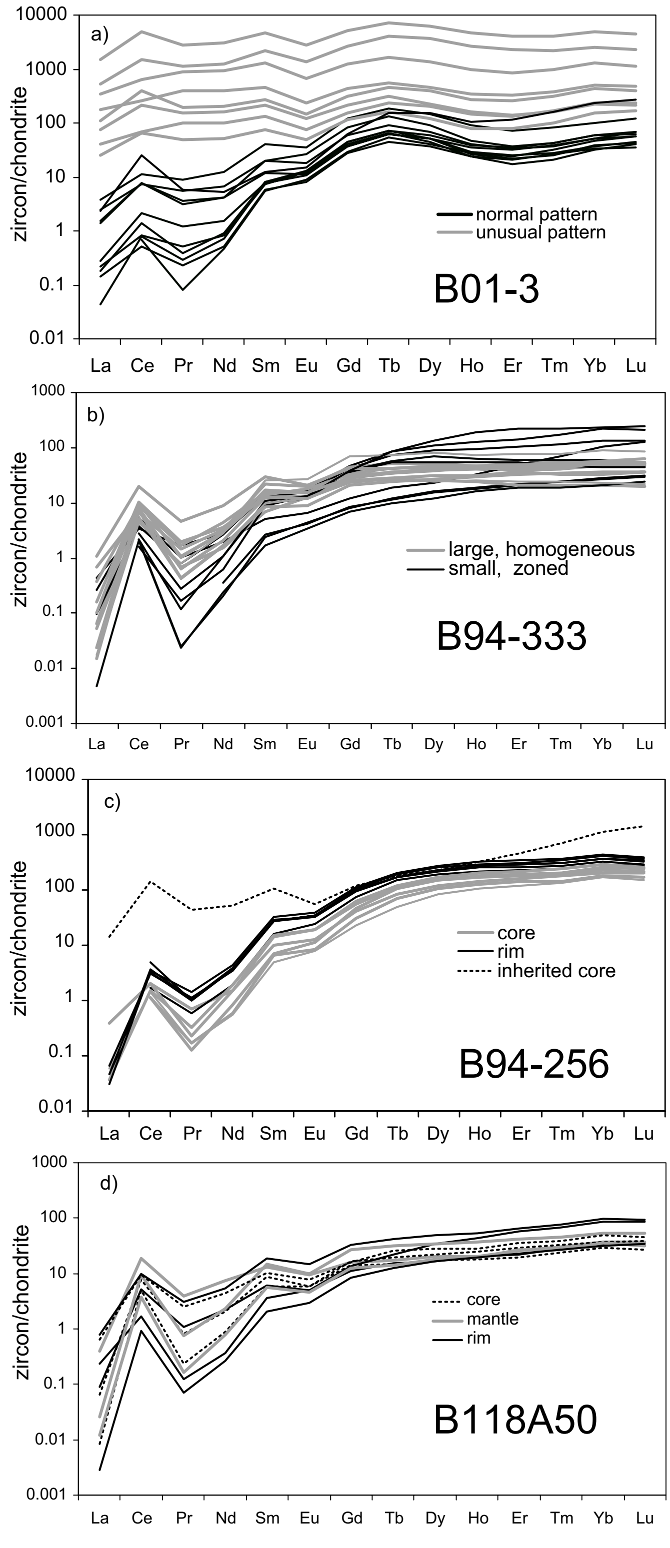
a)
B01-3
normal pattern
unusual pattern
zircon/chondrite
b)
B94-333
large, homogeneous
small, zoned
c)
B94-256
core
rim
inherited core
d)
B118A50
core
mantle
rim
La Ce Pr Nd Sm Eu Gd Tb Dy Ho Er Tm Yb Lu

Figure 11

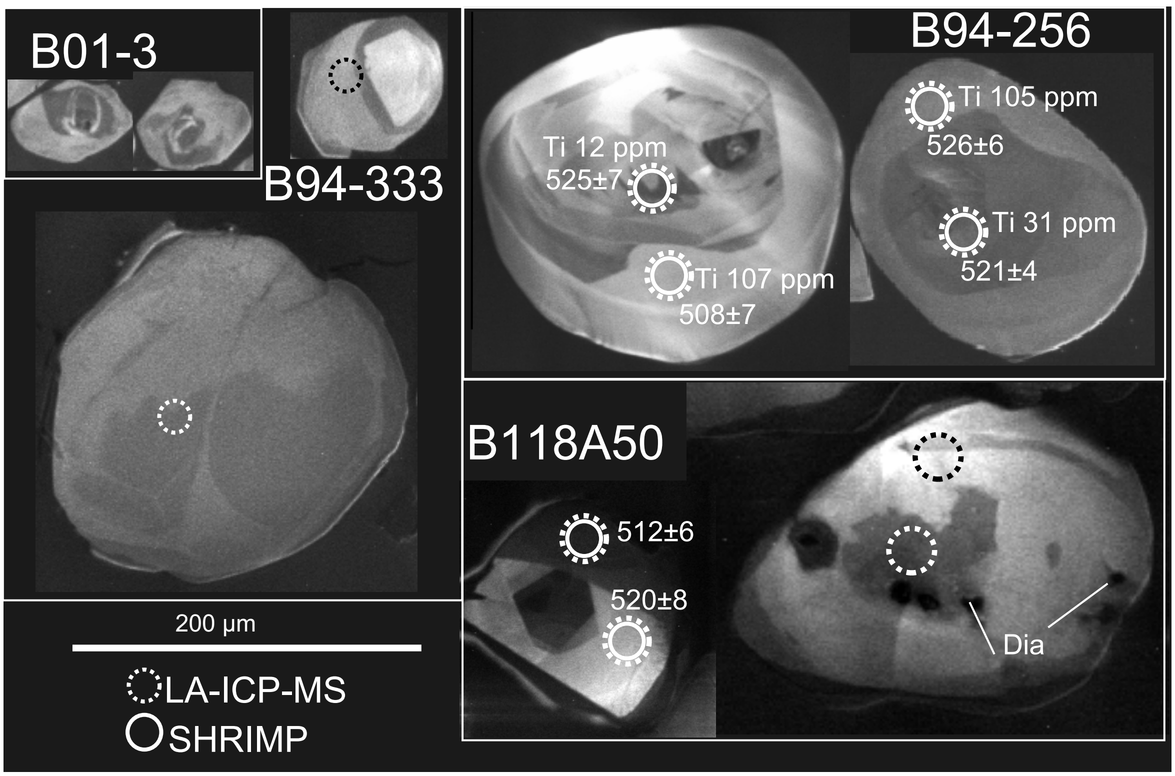
B01-3
B94-333
B94-256
Ti 105 ppm
526±6
Ti 12 ppm
525±7
Ti 31 ppm
521±4
Ti 107 ppm
508±7
B118A50
512±6
520±8
Dia
200 μm
LA-ICP-MS
SHRIMP

Figure 12

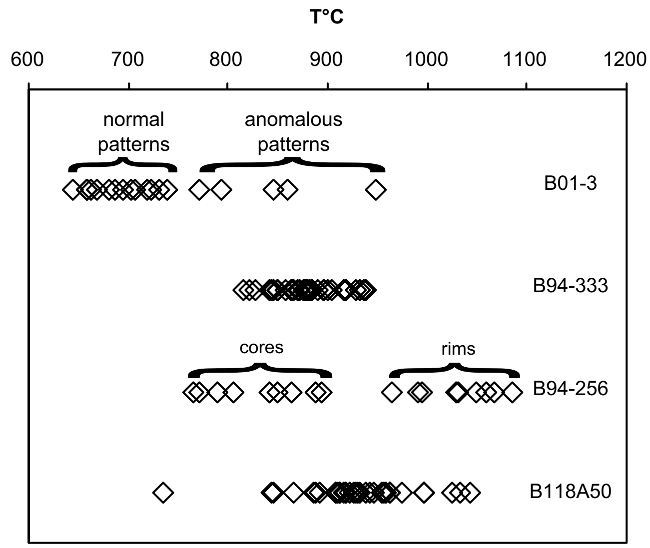
T°C
600
700
800
900
1000
1100
1200
normal patterns
anomalous patterns
B01-3
B94-333
cores
rims
B94-256
B118A50

Figure 13

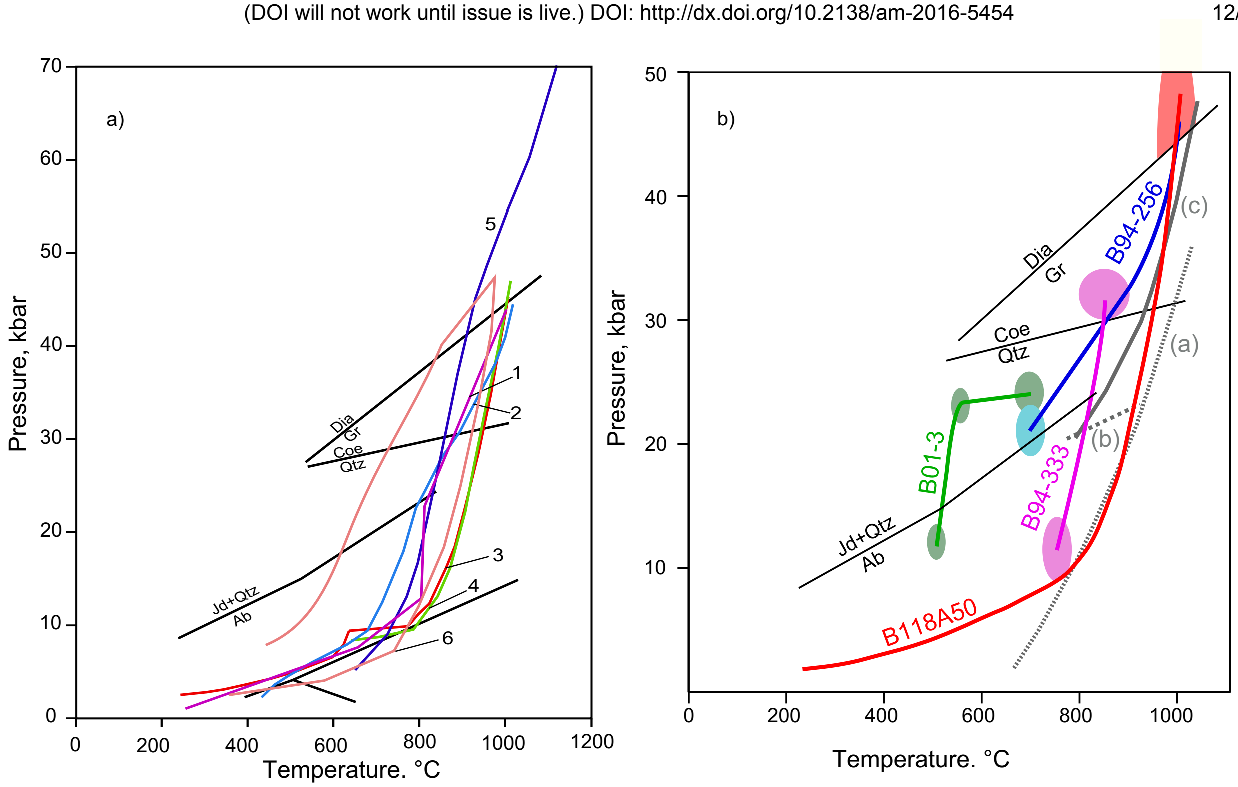
a)
Pressure, kbar
Temperature. °C
Dia
Gr
Coe
Qtz
Jd+Qtz
Ab
1
2
3
4
5
6
b)
B94-256
B94-333
B01-3
B118A50
(a)
(b)
(c)

Figure 14

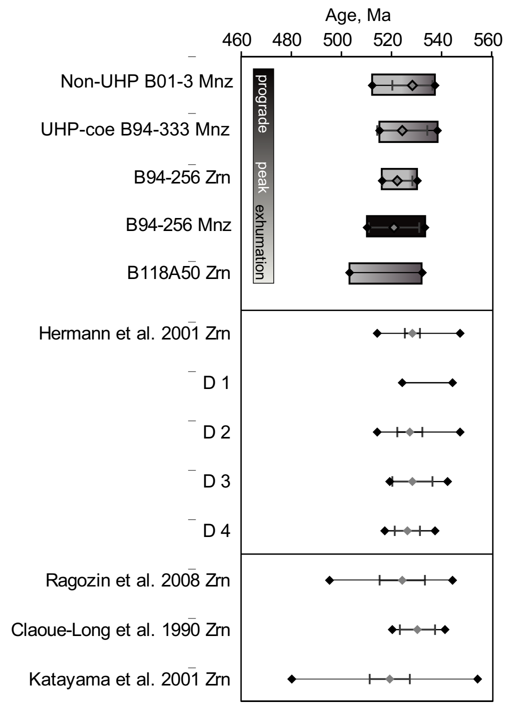
Age, Ma
460
480
500
520
540
560
Non-UHP B01-3 Mnz
UHP-coe B94-333 Mnz
B94-256 Zrn
B94-256 Mnz
B118A50 Zrn
prograde
peak
exhumation
Hermann et al. 2001 Zrn
D 1
D 2
D 3
D 4
Ragozin et al. 2008 Zrn
Claoue-Long et al. 1990 Zrn
Katayama et al. 2001 Zrn

Figure 15